

## Micro-pattern gaseous detectors in high-energy and astroparticle physics

Fabio Sauli

*CERN, CH-1211 Geneva, Switzerland*  
*fabio.sauli@cern.ch*

Received 26 August 2021  
Accepted 3 September 2021  
Published 12 October 2021

Introduced in the late 70s of the last century, a new generation of position-sensitive sensors named micro-pattern gaseous detectors (MPGDs) allows to detect and localize ionizing radiation with sub-mm accuracy and high-rate capability. Performing and reliable, MPGDs are gradually replacing detection systems based on multiwire proportional chambers, and find applications in particle physics, astrophysics, plasma diagnostics and other fields.

*Keywords:* Micro-pattern gas detectors; micro-strip gas chamber; MICROMEAS; gas electron multiplier.

### 1. Introduction

Since their introduction in the early years of the last century, gaseous radiation detectors have been developed with a variety of designs and performances, and are widely used in experimental particle physics and other applied fields. The invention by Charpak in the late 60s of the multiwire proportional chamber (MWPC),<sup>1</sup> providing fast information on energy and position of ionizing radiation over large sensitive volumes, revolutionized the field of detectors for particle physics, an achievement recognized by the assignment to Charpak of the 1992 Nobel Prize for Physics. Detection systems implementing gaseous detectors of various designs contributed to fundamental discoveries: the W and Z heavy vector bosons, the massive Higgs particle and many others.

Despite their large success, wire-based systems suffer, however, a loss of efficiency at radiation fluxes exceeding a few  $\text{kHz cm}^2$ ; they are, moreover, rather fragile and complex to manufacture. These limitations appeared particularly severe with the advent of high-luminosity colliders with their intense particle fluxes, added to the increasing difficulties to access the inner parts of large detectors to repair failures.

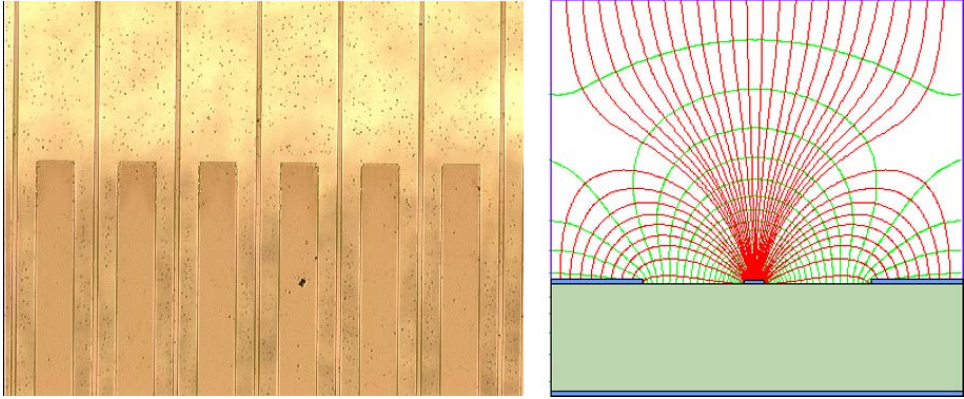


Fig. 1. Close view and electric field in the MSGC.

A promising alternative emerged in the late 80s with the development by Oed of the micro-strip gas chamber (MSGC),<sup>2</sup> having the active electrodes, anodes and cathodes, implemented as narrow metallic strips engraved on insulating substrates, in Fig. 1. Under the effect of the applied electric field, electrons released by ionization in the overlying layer of gas drift toward the plate and multiply in the high field near the thin anode strips.

Using high-resolution photolithography, distances between electrodes of a 100 microns or less could be reached, an order of magnitude smaller than in wire systems. Owing to the small pitch between electrodes and the fast collection on the near cathode strips of the positive ions created in the avalanche process, the rate capability of MSGCs extends the one of MWPCs by almost two orders of magnitude. The localization accuracy, obtained from a center-of-gravity algorithm on the charges recorded on neighboring electrodes, can reach 50  $\mu\text{m}$  or better.

While amply satisfying the rate and localization requirements met at the new machines, MSGCs failed, unfortunately, to pass the reliability requirements. Despite a large effort to improve the design, accidental radiation-induced discharges could severely damage the fragile anode strips. Originally foreseen to instrument the central tracker of the compact muon system (CMS) at CERN, they were ultimately replaced by solid-state devices. MSGCs have been successfully used in less demanding operating conditions, where lower gains are required, such as neutron spectrometers<sup>3</sup> and low-rate X-ray mapping in space applications.<sup>4</sup>

Inspired by the efforts to solve the problems encountered, novel detector structures have been developed from the late 90s, with comparable performances but increased reliability. These devices share the feature of narrow gaps between electrodes; on the application of suitable potentials, electron multiplication occurs in the high field, boosting the initial ionization charge. Realized with high-resolution photolithographic processes, they have been collectively named micro-pattern gaseous detectors (MPGDs). These developments are described in detail in a recent book of

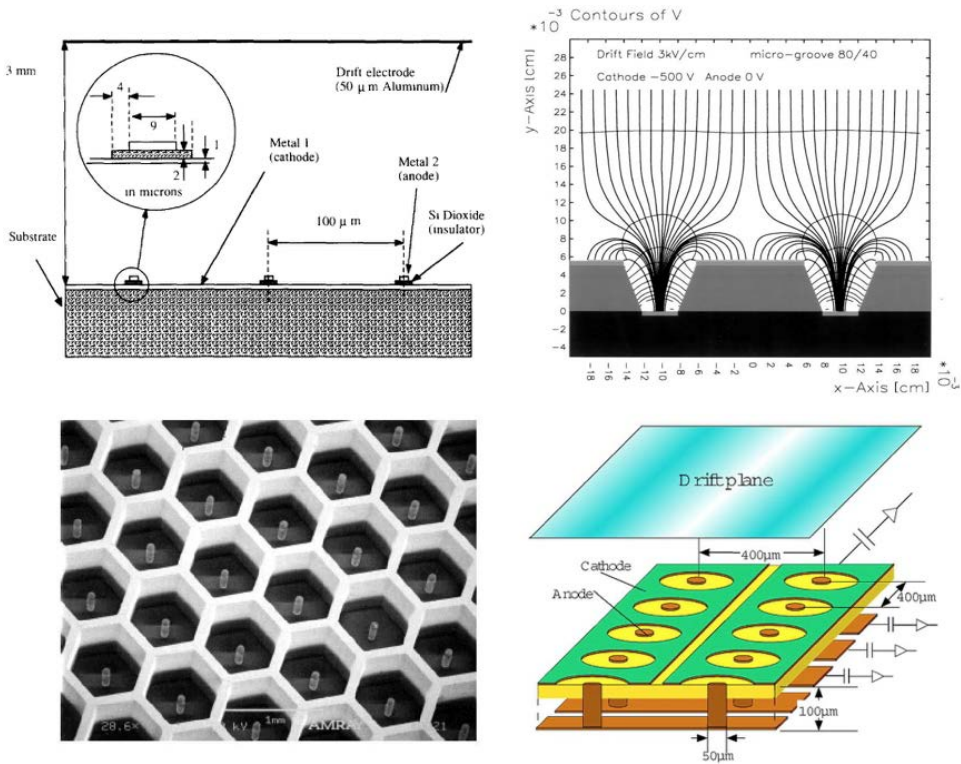


Fig. 2. Examples of MPGD structures. Top left to bottom right: Micro-gap chamber,<sup>8</sup> micro-groove detector,<sup>9</sup> micro-pin array,<sup>10</sup> micro-pixel detector.<sup>11</sup>

Sauli.<sup>5</sup> Some of the novel structures are shown in Fig. 2, a collation from different sources.

Two innovative designs, discussed in the following sections, have been particularly successful: the micro-mesh gaseous chamber (MICROME GAS)<sup>6</sup> and the gas electron multiplier (GEM)<sup>7</sup>; they are gradually replacing wire-based devices in a particle physics experiment, and find a variety of other applications.

The present note describes the conception and performance of selected detector systems in particle and astrophysics experiments making use of the novel MPGD devices.

## 2. MICROME GAS

### 2.1. Basic structure and performances

Introduced by Giomataris and collaborators in 1996, the MICROME GAS<sup>6</sup> consists of a thin-gap parallel multiplier separated from a sensitive or drift region by a grid. Functionally similar to the classic but unreliable parallel plate avalanche counters, the device's improved performance relies on the observation that a very

F. Sauli

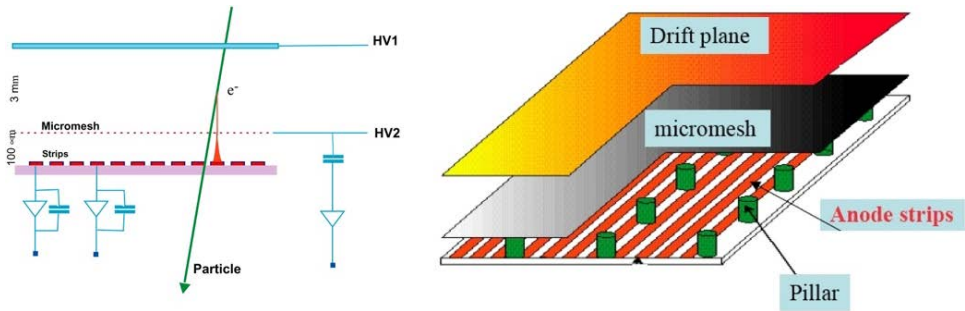


Fig. 3. Schematics of the MICROMEAS (left) and the pillars structure ensuring the gap uniformity (right).<sup>12</sup>

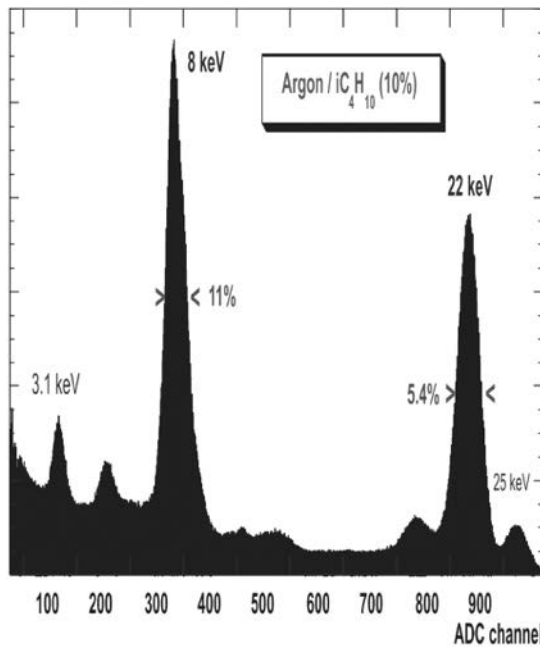


Fig. 4. Energy resolution for soft X-rays of a small-sized MICROMEAS.<sup>13</sup>

thin multiplication gap, typically 100 μm or less, permits to reach proportional gains well above 10<sup>3</sup> before the insurgence of discharges. As shown in Fig. 3, a fine metallic mesh separates multiplication and drift volumes; a set of built-in insulating pillars ensures the uniformity of the gap, essential for proper operation over large areas. Electrons released by ionizing radiation in the sensitive gap drift into the very high electric field between the mesh and the anode, multiply in an avalanche process and are collected by anode strips at a narrow pitch to perform localization.

Owing to the narrow gap, the detector can be operated in a range of voltages where the multiplication factor has a moderate dependence from the field, reducing

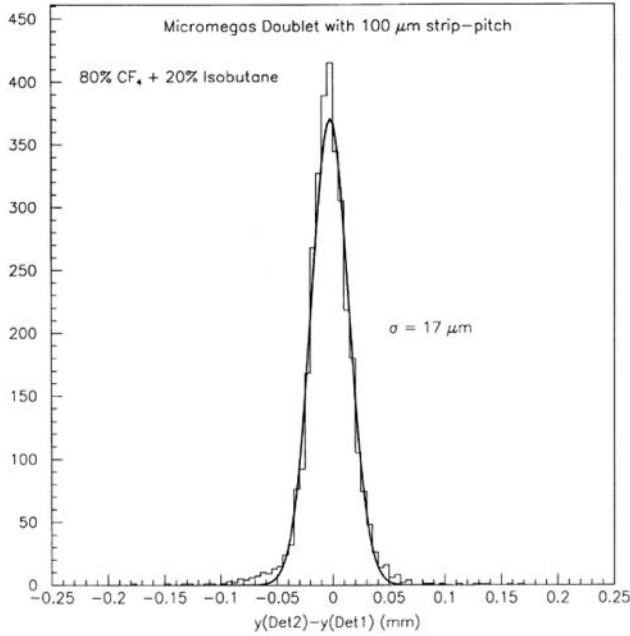


Fig. 5. Position accuracy for minimum ionizing particles perpendicular to the detector.<sup>14</sup>

the gain variations due to nonuniformities; as a result, the energy resolution in the detection of soft X-rays nears the statistical limit (Fig. 4).<sup>13</sup> Localization, obtained from a center-of-gravity estimate of the charge recorded on the anode strips, is also excellent; Fig. 5 is an example of best position accuracy measured for fast particles with a narrow gap MICROMEGAS operated with a low-diffusion gas.<sup>14</sup>

Various techniques have been devised to manufacture the insulating pillars ensuring the gap uniformity. Suited for the fabrication of large-area detectors, the so-called bulk MICROMEGAS makes use of commercially available metallic micro-meshes, laminated at high temperatures between two thin foils of photosensitive resin. After exposure to UV light through a suitably patterned mask, the excess resin is chemically removed, leaving a matrix of tiny pillars joining anode and mesh. While the presence of the pillars induces a local loss of efficiency, with the aspect ratio commonly adopted (a few hundred  $\mu\text{m}$  wide pillars at an mm pitch), the resulting loss is less than 1%.

MICROMEGAS devices are, however, prone to occasional discharges; while not damaging the structure, discharges introduce dead times in the operation. The problem is particularly severe on exposure to radiation fields containing heavily ionizing events, such as gamma-ray showers and neutron conversions. A solution has been found coating one electrode with a high-resistivity layer, whose effect is to induce a local drop of potential in case of a high current surge, choking the discharge.<sup>15</sup> For high radiation fluxes, however, the added resistance may cause a

F. Sauli

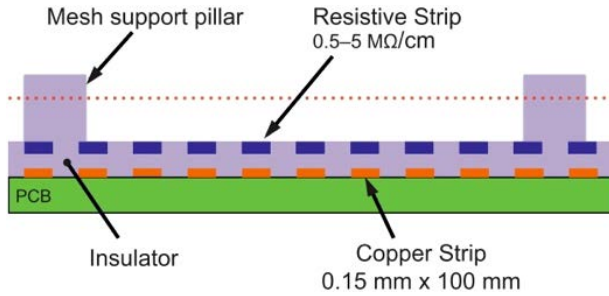


Fig. 6. Schematic structure of a resistive MICROMEAS.<sup>18</sup>

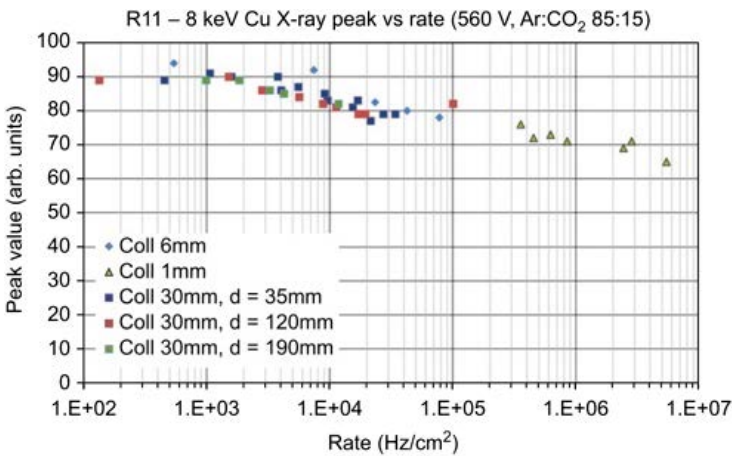


Fig. 7. Rate dependence of gain for anode strips resistivity of 2 MΩ/cm.<sup>18</sup>

drop of voltage, affecting the efficiency; the value of resistivity is a compromise between spark immunity and efficiency.<sup>16,17</sup> Figure 6 shows the structure of a resistive MICROMEAS. The multiplied charge is collected by resistive anode strips; signals are picked up by conducting strips capacitively coupled to the anodes. With a strip resistivity around 2 MΩ/cm, the detector's gain is unaffected up to an X-ray flux up to a few kHz/cm<sup>2</sup> (Fig. 7).<sup>18</sup>

### 3. Tracking in Particle Physics

A medium-scale system of MICROMEAS detectors has been operated as a beam tracker for the COMPASS spectrometer at CERN. The setup includes 12 identical devices, with an active area of 40 × 40 cm<sup>2</sup> each, mounted as pairs of chambers rotated by 90° to provide two-dimensional (2D) localization of the beam particles. With charge readout on anode strips at about 400 μm pitch, localization accuracies of 70 μm rms are achieved. Figure 8 shows two XY and UV detector doublets, mounted on the beamline, with the readout electronics boards.<sup>19</sup>

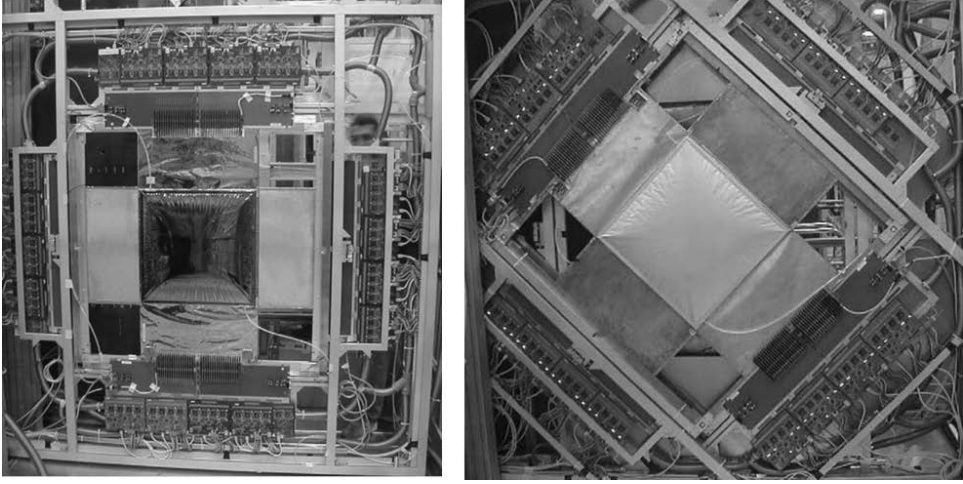


Fig. 8. MICROME GAS XY and UV doublet detector of the COMPASS spectrometer.<sup>19</sup>

With various improvements, the tracker has been operated successfully for more than a decade.<sup>20</sup> An ongoing development plans to upgrade the detector replacing the strip in the central section with a pixelized readout.<sup>21</sup>

To cope with the increased luminosity of CERN's LHC, resistive MICROME GAS devices have been chosen for tracking for the upgrade of the forward small wheel of the ATLAS muon spectrometer, replacing the present rate-limited detectors. The dual New Small Wheels (NSWs) complex, with a diameter of 10 m each, is divided into 16 sectors, 8 large and 8 small. Each detector module has four active layers, arranged as two doublets with readout strips at  $1.5^\circ$  to provide the 2D coordinates; five trapezoidal segments of variable sizes are supported by a common readout plane with strips at  $500 \mu\text{m}$  pitch mounted on a stiffening structure.<sup>22</sup> Figure 9 shows a large readout panel and an assembled prototype of

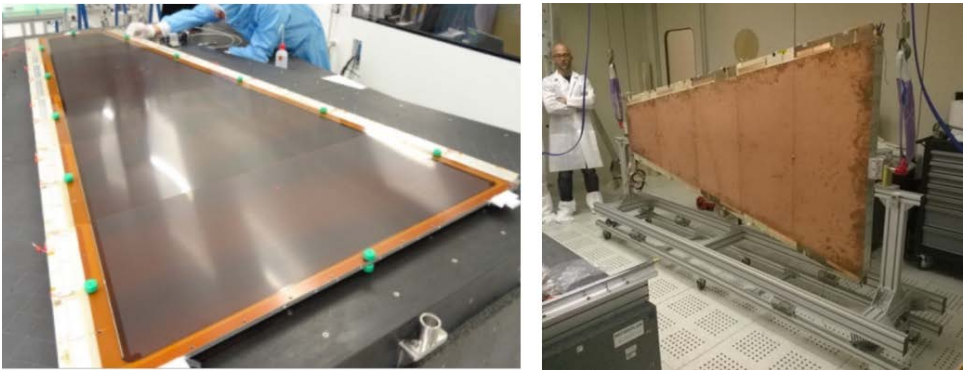


Fig. 9. A large MICROME GAS prototype for the ATLAS NSW in construction.  
Source: CERN.

*F. Sauli*

the MICROME GAS module. The completed detectors are assembled between two thin-gap chambers, having better timing but coarser localization, and used for triggering; Fig. 10 illustrates the installation of a complete module on the NSW.

After extensive testing of the prototypes at CERN,<sup>23</sup> the manufacturing of the full system, comprising 128 large modules is shared between contributing laboratories<sup>24</sup> and will be installed during the LHC upgrade shutdown.



Fig. 10. Installation of a MICROME GAS-thin-gap chamber module on the NSW.  
Source: CERN.

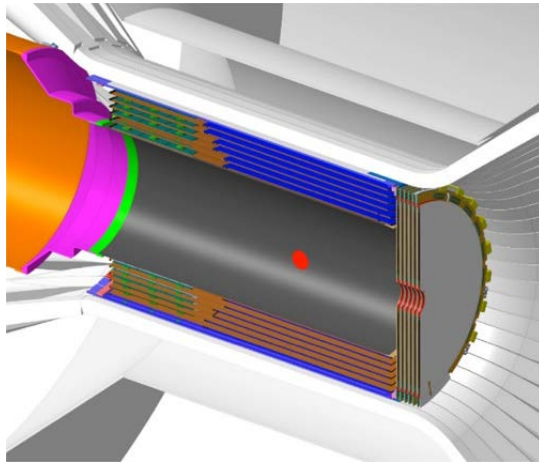


Fig. 11. The CLAS12 six cylindrical and six forward MICROME GAS detectors.<sup>25</sup>

While the majority of MICROME GAS devices are planar, a system of cylindrical detectors has been built and operated in the CLAS12 experiment at the Jefferson laboratory. The barrel MICROME GAS tracker has six layers of cylindrical detectors: three with strips along the beam axis, providing the azimuthal angle of the particle, and three with circular strips perpendicular to the beam axis, improving the polar angle determination (Fig. 11). Figure 12 is an example of a five-prong recorded event.<sup>25</sup>

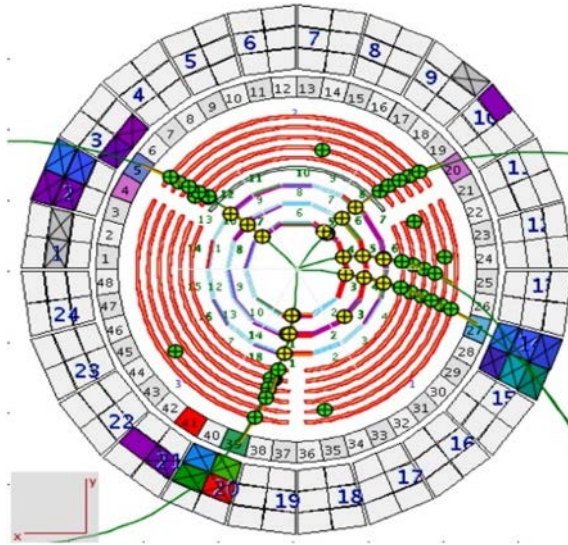


Fig. 12. A five-prong event recorded with the barrel detector.<sup>25</sup>

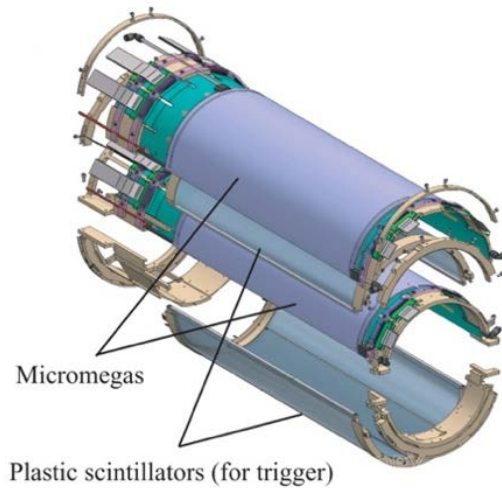


Fig. 13. Schematic view of the AMT.<sup>27</sup>

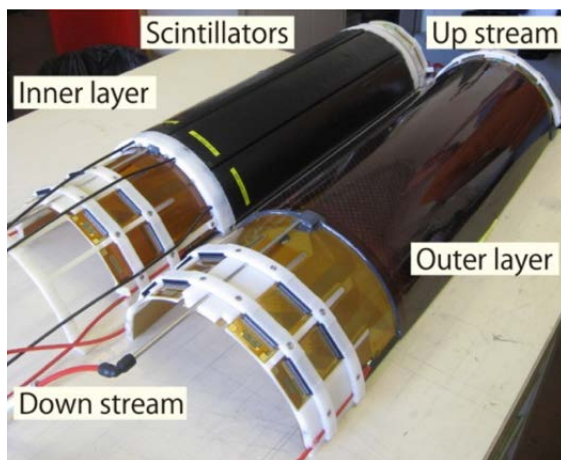


Fig. 14. Half-cylinder MICROMEAS.<sup>26</sup>

Another example of cylindrical structure is the ASACUSA<sup>a</sup> MICROMEAS tracker (AMT) used to record antiproton–nucleon annihilation vertices at CERN’s antiproton decelerator complex. Built as a cylindrical layer of plastic scintillator bars, sandwiched between two half-cylinder MICROMEAS, the detector has an overall length of 61.5 cm; sets of parallel strip anodes are used to record the signals (Figs. 13 and 14).<sup>26, 27</sup>

#### 4. Readout of Time Projection Chambers

The time projection chamber (TPC), developed in the late 70s, is a powerful gaseous detector providing full 3D images of complex events interacting in a large sensitive volume.<sup>28</sup> A TPC consists of a large gas-filled box or barrel, equipped at one end with an array of multiwire chambers for the detection and localization of ionizing trails; continuous recording on wired and cathode pads of charge and time of arrival of the track segments permits to reconstruct the events. For an overview of performances and experiments instrumented with the device see, for example, Chap. 10 of the Sauli’s book on gaseous radiation detectors.<sup>29</sup>

The excellent linearity of response and energy resolution of the MICROMEAS suggested the use of the device in experiments where an accurate measurement of the differential energy loss is paramount for particle identification. A system of modular TPCs with MICROMEAS readout was built and operated as part of the near detector complex of the Tokay-to-Kamioka (T2K). In each module the endcap is equipped in a matrix of 12 bulk MICROMEAS plates with the anode segmented in  $\sim 1700$  rectangular pads with individual charge and time recording (Fig. 15);

<sup>a</sup>Atomic spectroscopy and collisions using slow antiprotons.

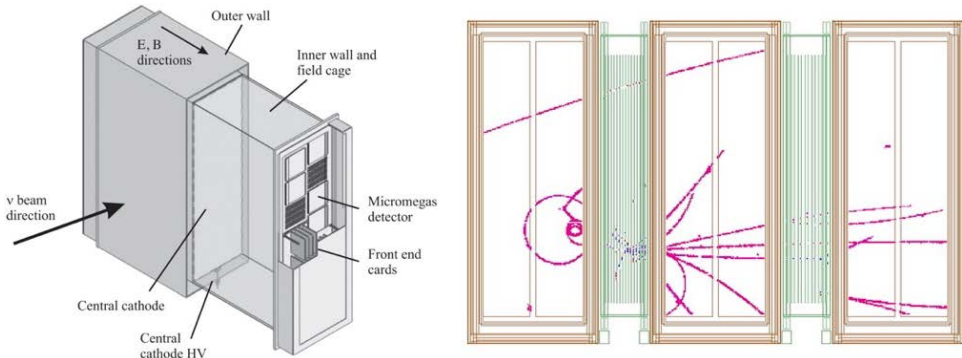


Fig. 15. A MICROMEAS-TPC module of the T2K experiment and a multi-track event due to a neutrino interaction.<sup>30</sup>

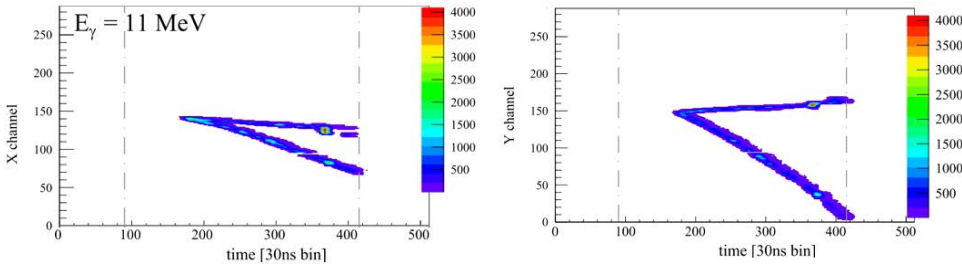


Fig. 16. Electron-positron pair from a 11 MeV gamma recorded in the X and Y projections with the HARPO TPC.<sup>32</sup>

on the left, a recorded multi-tracks event originating from a neutrino interaction in front of the first TPC module.<sup>30</sup>

An upgrade of the T2K complex is under development, making use of resistive MICROMEAS for the TPC endcap readout.<sup>31</sup>

Developed for gamma-ray astronomy and polarimetry, the HARPO MICROMEAS TPC is a smaller volume device dedicated to the detection of gamma-rays from the MeV to the TeV energy regions. Operated at pressures up to 5 bars, the cubic vessel, 30 cm on the sides, has the anode plane patterned with alternating strips and interconnected pads to perform 2D localization.<sup>32</sup> Figure 16 is an example of gamma-ray conversion recorded in the X and Y projections.

## 5. Miscellaneous Applications

MICROMEAS devices are used as detectors in a variety of applications, particularly owing to their good energy resolution. A few are briefly mentioned here; the reader is directed to the quoted references for more information:

- “Muography” is a method to explore the internal structure of massive bodies recording the modulations of the cosmic muon flux traversing the target; it is

F. Sauli

used to investigate the presence of hidden chambers in the Khufu's pyramid.<sup>33</sup> A high-resolution muon tomography system aiming at industrial applications is under development.<sup>34</sup>

- The CAST experiment: It is used as a detector of X-rays emitted by the hypothetical solar axions by Primakoff effect.<sup>35</sup>
- With thin  ${}^6\text{Li}$  and  ${}^{10}\text{B}$  converter layers deposited on the cathode plane for the detection and localization of neutron.<sup>36–38</sup>
- CALISTE-MM: It is an X-ray polarimeter for applications in astrophysics.<sup>39</sup>

## 6. The Gas Electron Multiplier

### 6.1. Basic structure and performances

The GEM, introduced by Sauli in 1997, is a thin polymer foil metal-coated on both sides and pierced with a high density of holes, typically  $50\text{--}100\text{ mm}^{-2}$  (Fig. 17).<sup>40</sup> Inserted between a cathode and a charge collecting anode, on the application of appropriate potentials, the GEM electrode develops the field lines and equipotential shown in the figure. The large difference of potential applied between the two faces of the foil creates a high field in the holes; electrons released in the upper region drift into the holes acquiring sufficient energy to initiate ionizing collisions with the molecules of the gas filling the structure. A sizeable fraction of the electrons produced in the avalanches leaves the multiplication region and transfers into the lower gap of the structure, where it can be collected by an electrode or injected into a second multiplying section. This gives the detector unique flexibility of use, exploited to achieve higher gains and better performances.

Small- and medium-sized GEM electrodes are fabricated with a double-mask, high-quality wet etching technique, using high-grade polyimide foils coated on each side with a thin metal layer (in most cases,  $50\text{ }\mu\text{m}$  thick Kapton with  $5\text{ }\mu\text{m}$  copper

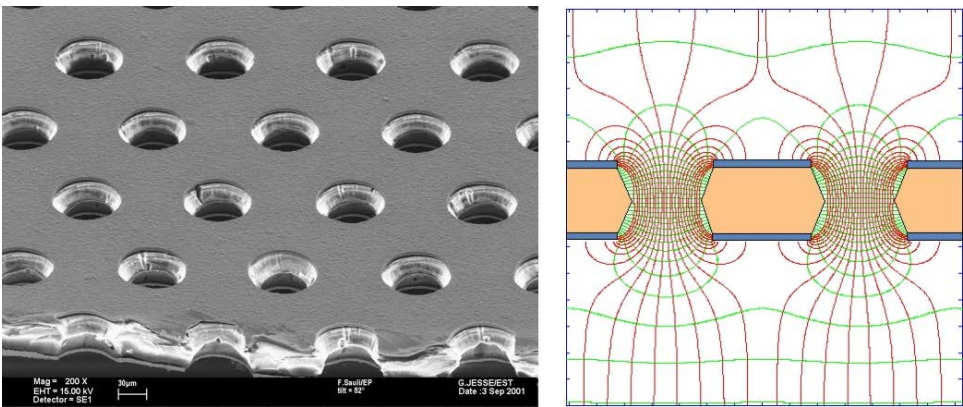


Fig. 17. Electron microscope view and electric field in the GEM electrode.

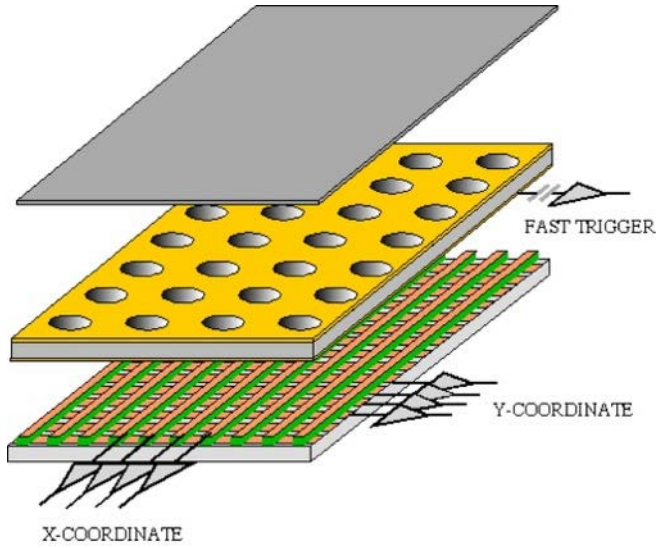


Fig. 18. Schematics of a single-GEM detector, with two sets of perpendicular strips for the signal readout.<sup>43</sup>

claddings). The foil, coated with a photosensitive resin layer, is exposed from both sides to UV light through masks with the holes' pattern; the exposed resin is chemically removed with a standard printed circuits technology. The metal is then etched in an acid bath and the foil immersed in a solvent for the polymer until holes dig in from the two sides, resulting in a characteristic double-conical shape, also named hourglass.<sup>b</sup> The diameter and shape of the holes influence the performance and long-term stability of a detector. To ensure high gains, their optimum diameter should be comparable to the foil thickness; a common choice for 50  $\mu\text{m}$  thick polymer foils is  $\sim 70 \mu\text{m}$  diameter at 140  $\mu\text{m}$  pitch.<sup>41</sup>

The maximum proportional amplification that can be attained with a GEM foil depends on the gas used and manufacturing quality; for electrodes of small sizes, an effective gain above  $10^3$  can be attained.<sup>42</sup> Figure 18 shows schematically a single-GEM detector, with the anode patterned for X- and Y-projective coordinate readout; an opposite polarity signal is detected on the lower GEM side, providing a trigger for neutral radiation. The energy resolution for the  $^{55}\text{Fe}$  5.9 keV line is around 17% FWHM.

To satisfy the stringent requirements on diameter and pitch of the holes, the two masks have to be aligned with a tolerance of a few microns, an increasingly difficult requisite for large sizes. A single mask process has been developed to permit the realization of larger areas, up to and above a square meter<sup>44</sup> and is being used to manufacture the large tracker detectors discussed below.

<sup>b</sup>Processes developed by Rui De Oliveira and collaborators (CERN Detector Technologies).

Alternative production methods have been developed, such as plasma etching and laser drilling<sup>45,46</sup>; they have limited use due to high manufacturing costs. Mechanical drilling on thicker supports has been employed to manufacture devices entailing coarser performances: the so-called optimized GEM,<sup>47</sup> thick GEM (TH-GEM)<sup>48,49</sup> and large electron multiplier (LEM)<sup>50</sup> are suitable for applications requiring large-area, rigid electrodes, as photosensitive detectors and cryogenic devices.

Single-GEM electrodes can reach gains well above  $10^3$  when tested in favorable laboratory conditions. However, as for other micro-pattern devices, when exposed to high rates and/or harsh beam environments they tend to discharge at lower values of gain. Differently, however, from all previously described MPGDs, GEM electrodes can be assembled in cascade, achieving large amplifications at moderate operating voltages for each element; this results in a substantial reduction of the discharge rates for equal gains.<sup>51</sup> While double- and triple-GEMs devices are the most widely used, cascades of up to five electrodes have been tested.<sup>52,53</sup> Figure 19 shows schematically a triple-GEM structure, with a simple resistor chain providing the appropriate voltages to the different electrodes. Figure 20 provides an example of gain measured with multiple GEM devices; the maximum values correspond to the discharge limit.<sup>51</sup>

In multiple structures, while the GEM voltages determine the overall gain, the electric fields in the transfer and induction gaps control the flow, spread and collection of the electron and ion charges. A thorough optimization of the various field strengths permits to achieve the optimum operating performances in terms of gain, ion backflow reduction and discharge rates. Dedicated programs have been used to simulate the multiplication and transfer processes in a variety of conditions, geometry, gas fillings, presence of an external magnetic field: MAGBOLTZ to compute the electron and ion drift velocity and avalanche multiplication,<sup>54</sup> GARFIELD to map the electric fields and motion of the charges.<sup>55,56</sup>

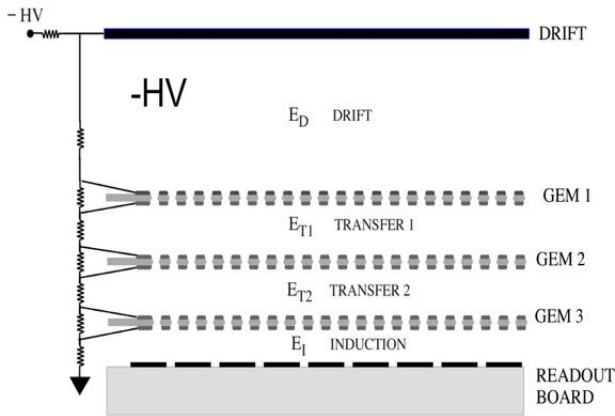


Fig. 19. Scheme of a triple-GEM with the resistor chain used to power the electrodes.

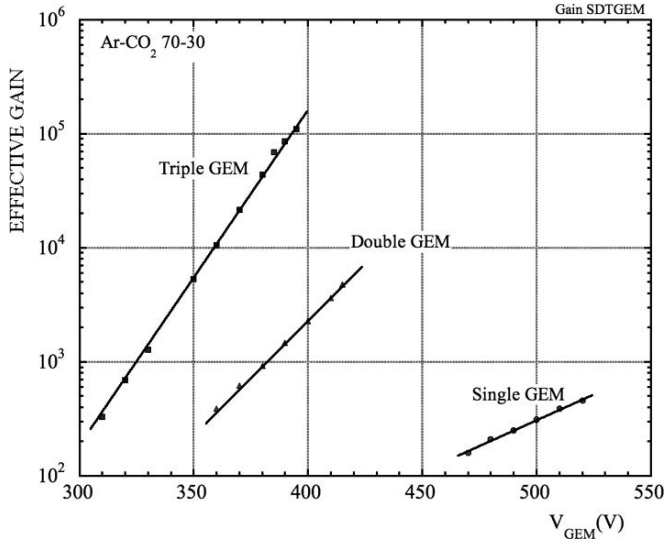


Fig. 20. Measured gain for single-, double- and triple-GEM detectors as a function of the voltage applied to each electrode.<sup>51</sup>

## 6.2. GEM-based trackers in particle physics

A popular detector construction method (the “box” assembly) for prototype developments and moderate sizes makes use of a set of frames serving the different functions and assembled with bolts and O-rings. Drift and GEM electrodes are stretched on tensioning frames and glued on the final fiberglass frames; the anode with the readout pattern is manufactured on a thin printed circuit board and serves also as a gas window.<sup>43</sup> For larger detector sizes, a monolithic assembly has been developed for the tracker of the COMPASS spectrometer at CERN. The structure makes use of thin mechanically-cut fiberglass frames with narrow spacer inserts at regular intervals; pre-stretched GEM foils, 30 cm on the side, are glued onto the frames serving both as support and spacer to the next electrode (Fig. 21).<sup>57</sup> One side of the large GEM foils is divided into sectors, individually connected to the voltage through a high-value resistor to limit the energy available in case of a spark. As a rule of thumb, the surface of each sector should not exceed around 100 cm<sup>2</sup>, corresponding for a 50  $\mu$ m Kapton foil to a capacitance of about 5 nF.<sup>51</sup> A central circular sector with independent powering can be used to inhibit detection in the beam region in the highest intensity runs.

The picture in Fig. 22 shows the author holding one of the medium-sized GEM foils manufactured at CERN for the COMPASS tracker; Fig. 23 is a view of one of the detectors installed in the M2 beamline of the spectrometer; each module provides the 2D coordinates of charged tracks with 70  $\mu$ m accuracy and 10 ns time resolution. Twenty-two identical devices were built and operated from 2004 until the LHC shutdown.

F. Sauli

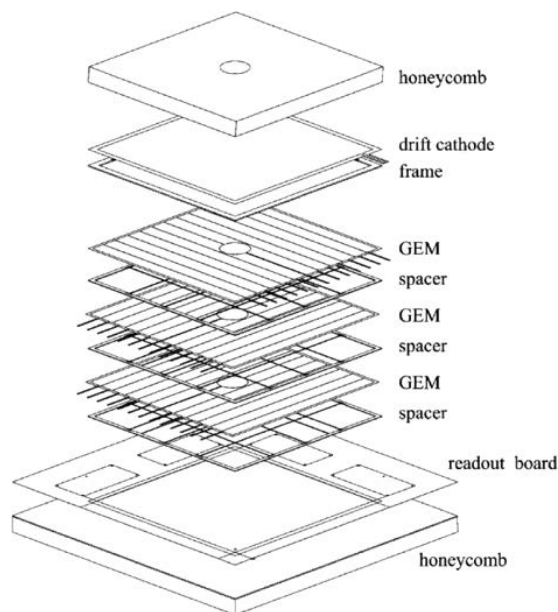


Fig. 21. Exploded assembly scheme of the COMPASS triple-GEM module.<sup>57</sup>



Fig. 22. The author with one of the GEM electrodes used for the COMPASS triple-GEM tracker.  
Source: CERN.

A similar construction scheme has been adopted for the forward tracker of the TOTEM experiment at CERN; in this case, the triple-GEM detectors have a semi-circular shape to match the experimental requirement, illustrating the flexibility of the technology. Figure 24 is a view of one half of the assembled TOTEM telescope, mounting 10 GEM chambers in sequence.<sup>58</sup>

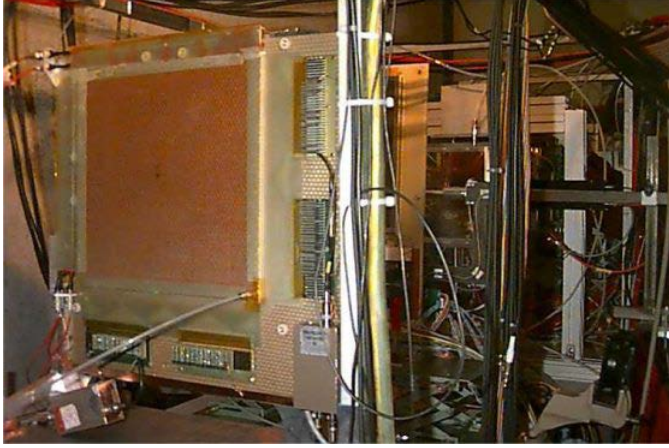


Fig. 23. One of the GEM detectors in the COMPASS beamline. *Source:* CERN.

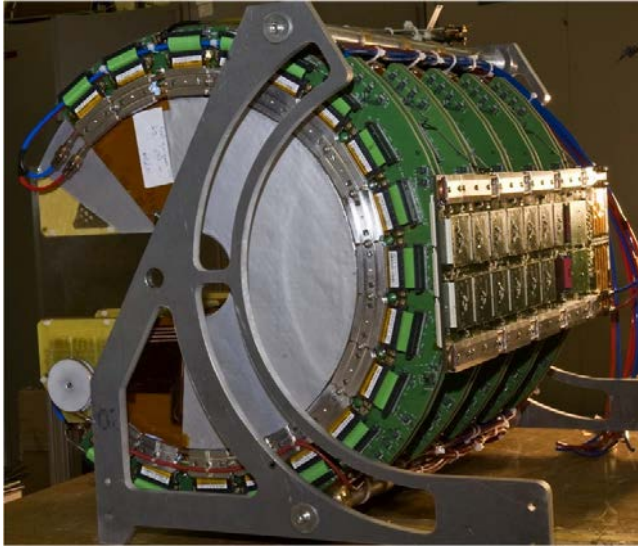


Fig. 24. One module of the TOTEM tracker mounting 10 semi-circular triple-GEMs.<sup>58</sup>

The flexibility of the GEM electrodes permits the construction of nonplanar devices; as charge multiplication occurs in the holes, bending of the foil does not modify the main detector properties. A four-layer cylindrical GEM detector, with an active length of 70 cm and built for the KLOE-2 inner tracker in Frascati, is shown in Fig. 25.<sup>59</sup> The readout pattern, with longitudinal and interleaved strips at  $25^\circ$ , provides a spatial resolution of 200 and 400  $\mu\text{m}$  rms for the azimuthal and longitudinal coordinates, respectively.

F. Sauli



Fig. 25. Four-layer cylindrical GEM detector for the KLOE-2 inner tracker in Frascati.<sup>59</sup>

Developed both to serve as target and tracker at Jefferson lab, the BoNus detector is a radial TPC with three cascaded curved GEM amplifiers; the readout is performed on rows of pads on the outer cylinder.<sup>60</sup> A cylindrical triple-GEM device has been built also for the inner tracker upgrade of the BESIII experiment at IHEP in Beijing.<sup>61</sup>

Suitable for medium-sized detectors, the COMPASS construction is not well suited to manufacture larger devices since internal parts cannot be accessed in case of failure. A new assembly technique has been developed for the construction of the CMS high- $\eta$  muon detector upgrade at CERN; named “self-stretching”, it relies on the use of rigid support frames with a system of screws and bolts to tension the GEM foils all around their edges (Fig. 26).<sup>62</sup> Figure 27 is an exploded view of the

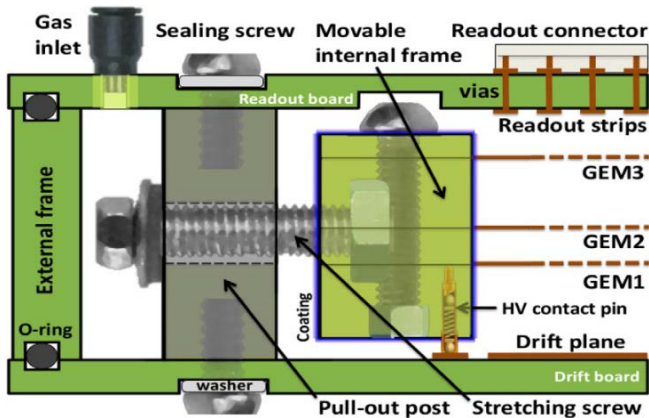


Fig. 26. The system of screws and bolts used to tension the GEM foils on rigid frames.<sup>62</sup>

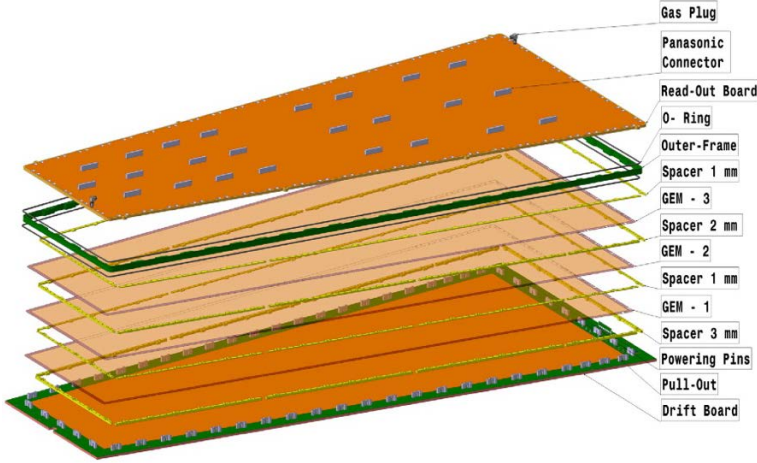


Fig. 27. Blow up of a large triple-GEM module of the CMS forward muon detector.<sup>63</sup>

assembly<sup>63</sup> and Fig. 28 shows various steps in the assembly sequence. Prototypes underwent extensive testing in view of the final product in various participating institutes.<sup>64</sup>

Figure 29 shows the installation of the first GEM station on the forward muon detector supporting wheel; the full assembly includes 160 triple-GEM modules and will be operational at the start-up of CERN's high-luminosity large hadron collider.

### 6.3. GEM readout of time projection chambers

For the reasons discussed in Sec. 4, the increasing event rates and particle multiplicities have demanded the replacement of classic multiwire chamber readouts with the more powerful MPGD structures in TPCs; single- or multi-GEM readout structures are particularly attractive because of large gains and flexible geometry. Extensive development work in this direction was originally motivated by the studies of detector systems for the planned international linear collider project.<sup>65</sup> In view of the size of the devices, requiring a large number of readout channels, detailed studies on the optimal geometry, size and shape of the pads have been performed.<sup>66,67</sup> Recording of the collected charge on all pads and using suitable interpolating algorithms, single track position accuracies in the XY projection of  $\sim 150 \mu\text{m}$  rms have been achieved, decreasing to  $\sim 400 \mu\text{m}$  for 1-m drift length, due to electron diffusion. In a 4 T magnetic field, parallel to the drift direction, the position accuracy remains below  $200 \mu\text{m}$  up to the maximum drift length.<sup>68</sup>

Developed for the PANDA experiment, the GEM-TPC depicted in Fig. 30 was extensively tested in the framework of the FOPI spectrometer at GSI, Darmstadt.<sup>69</sup> With  $\sim 30$  cm active outer diameter and 73 cm length, the detector fits into the central drift chamber of the experiment. Optimized for operation in high magnetic fields, it operates with a low-diffusion Ne-CO<sub>2</sub> (90-10) gas mixture; signals

F. Sauli

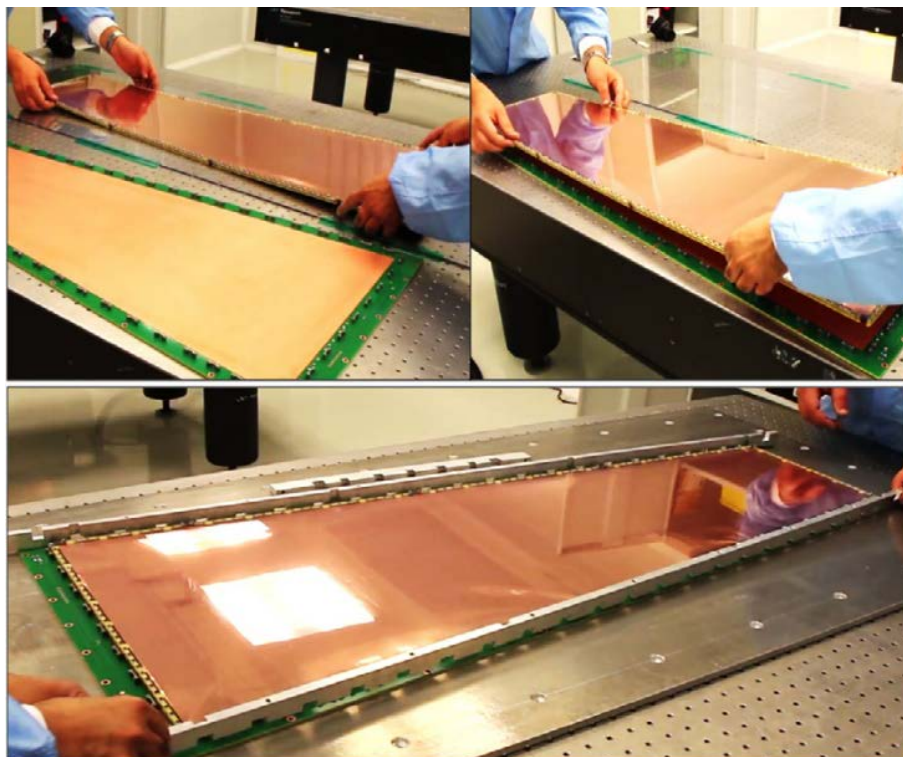


Fig. 28. Several steps in the assembly sequence of the GEM CMS upgrade detectors.<sup>64</sup> *Source:* CERN.

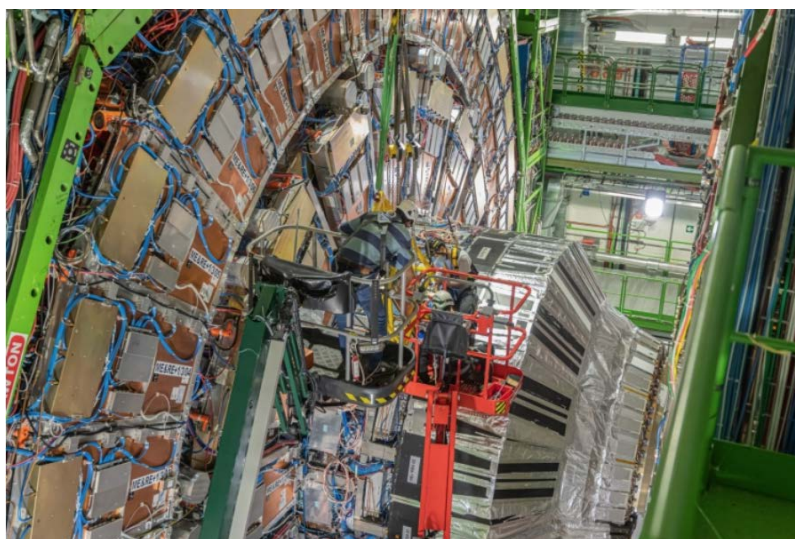


Fig. 29. Installation of the first GEM station on the CMS forward muon detector. *Source:* CERN, 2019.

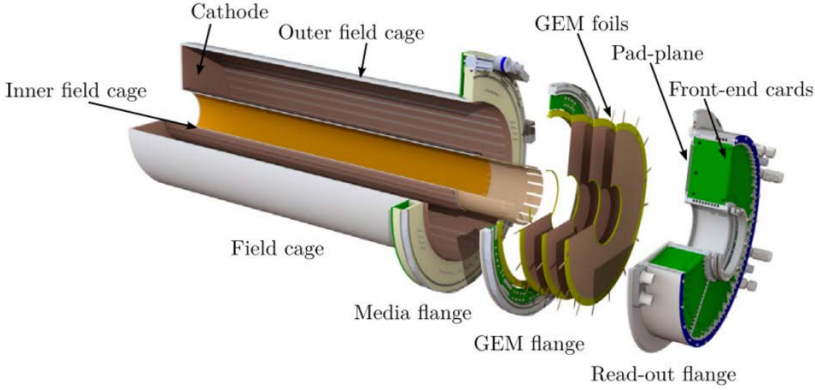


Fig. 30. The PANDA GEM-TPC detector for FOPI.<sup>69</sup>

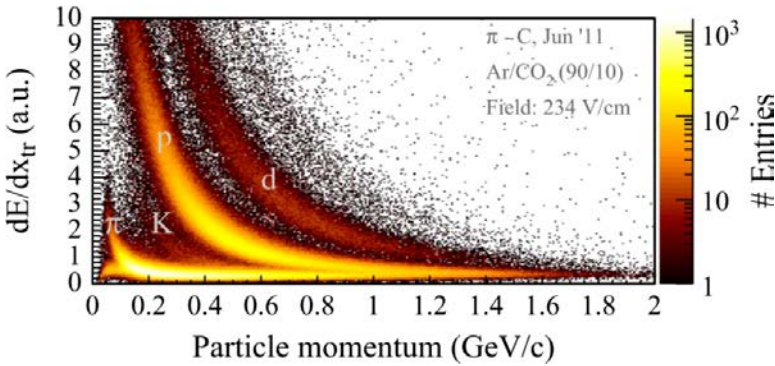


Fig. 31. Differential energy loss of charged particles recorded with the PANDA GEM-TPC.<sup>70</sup>

are readout on a matrix of  $\sim 10,000$  pads, with an outer diameter of 1.5 mm.<sup>69</sup> Figure 31 demonstrates the excellent particle identification properties of the device obtained from the correlation between measured momentum and differential energy loss.<sup>70</sup>

The ALICE experiment at CERN has completed the construction of a GEM-TPC upgrade to match the increased LHC luminosity. The improved detector uses the existing field cage, replacing the MWPC endcap with a GEM-based readout (Fig. 32).<sup>71</sup> A quad-GEM cascade, with alternating electrodes having the hole's pattern with different pitches (Fig. 33), has been optimized to reduce below 1% the ions backflow into the large drift volume, a source of field distortions.<sup>72</sup> The 18 segments on each endcap are equipped with four-GEM modules, 160 cm long, seen in Fig. 34 (Ref. 73); Fig. 35 shows one ALICE TPC endcap in the course of replacement of a MWPC sector by one GEM module. Production, testing and assembly of the 72 quad-GEM modules have been completed at the time of writing.

F. Sauli

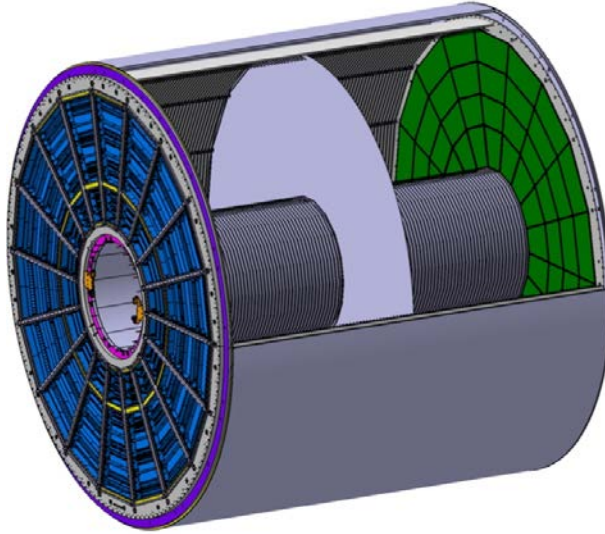


Fig. 32. The ALICE TPC with GEM readout.<sup>71</sup>

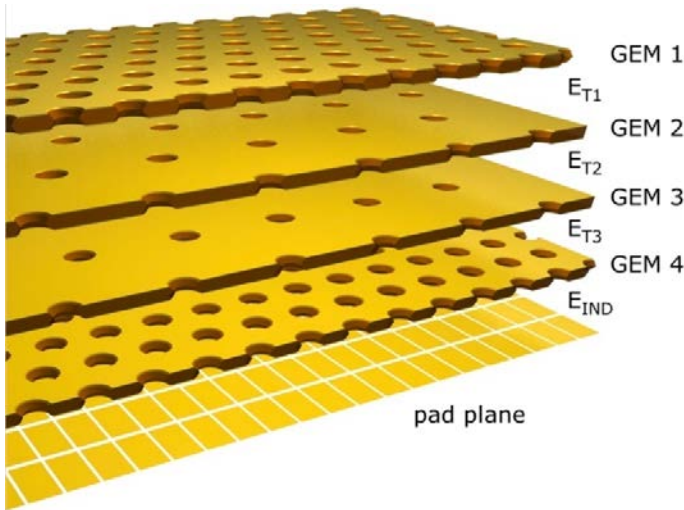


Fig. 33. Schematics of the quad-GEM stack adopted to reduce the positive ions backflow.<sup>72</sup>

#### 6.4. UV photons detection and localization

The high gains and good localization properties achievable with gaseous devices permit the detection of single photoelectrons. Originally implemented using wire chambers filled with a photosensitive vapor, the technology has progressed with the introduction of the MPGD detectors and the development of solid-state photocathodes. Various attempts have been made to develop gas-compatible photocathode

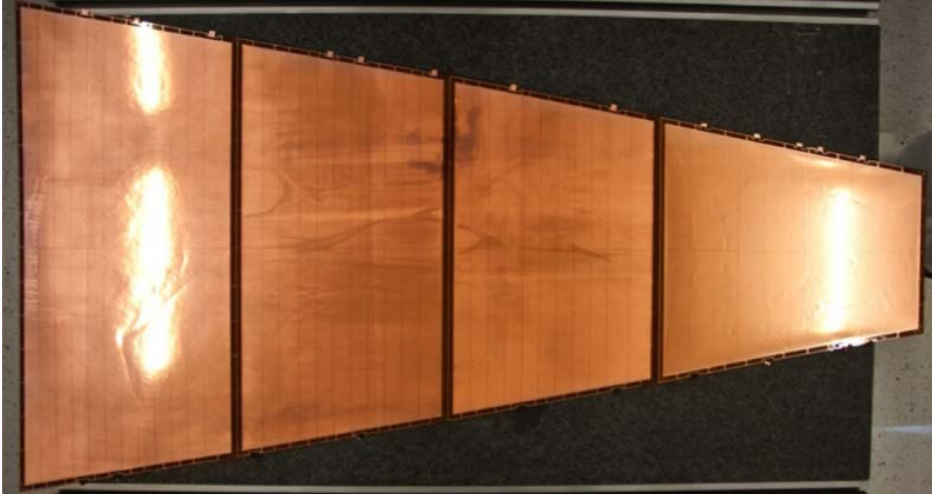


Fig. 34. A prototype assembly of four GEM modules for the ALICE GEM-TPC.<sup>73</sup>



Fig. 35. A three-module GEM panel being mounted on the outer readout chamber of the ALICE TPC upgrade. *Source:* CERN, 2019.

materials sensitive in the visible range; however, most gaseous photon detectors make use of thin layers of caesium iodide deposited on electrodes, sensitive in the UV; CsI has an ionization threshold of 5.9 eV and a quantum efficiency reaching  $\sim 30\%$  before transparency cut-off of the best UV windows, 10–11 eV. Particularly suited to achieve high gains, a multi-GEM device with the photosensitive layer

F. Sauli

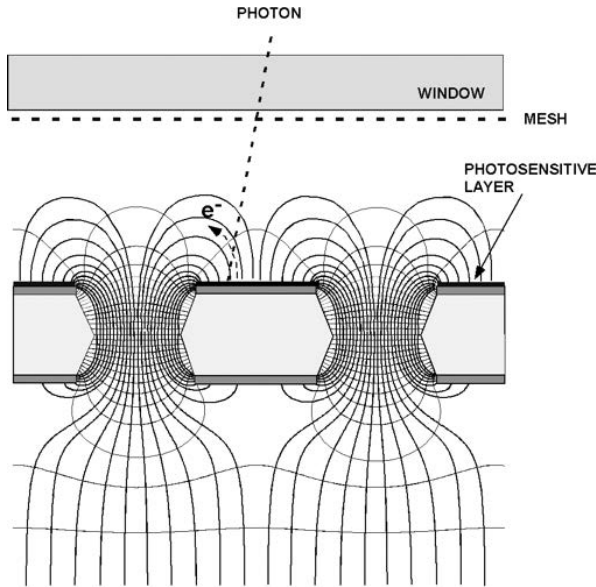


Fig. 36. “Inverted” photocathode: the first GEM in a cascade is coated with the photosensitive layer.<sup>74</sup>

deposited on the first electrode side facing the window has the further advantage to strongly suppress the gain-limiting effect of feedback of photon and ion generated by the following amplification stages, (Fig. 36). Figure 37 is an example of localization accuracy for single UV photons for a collimated photons beam perpendicular to the detector; the coordinate is deduced with a center-of-gravity calculation on the charge recorded on 200  $\mu\text{m}$  wide anode strips.<sup>74</sup>

These developments opened the possibility to build window-less threshold Cherenkov counters, sensitive to electrons with good rejection of heavier particles.<sup>75</sup> The PHENIX hadron blind detectors (HBDs) at RHIC consists of a cylindrical TPC-like detector surrounding the beam intersection region, filled with  $\text{CF}_4$  at atmospheric pressure as Cherenkov radiator (Fig. 38).<sup>76</sup> Photons emitted in the radiator by charged particles are detected and localized in a set of triple-GEM amplifiers, with the first, facing the radiator, coated with a CsI photosensitive layer; the photons are contained within a wide spot, or blob, with a radius depending on the Cherenkov angle.

Similar in conception, the HBD developed for the J-PARK E16 experiment to discriminate electrons from pions makes use of a CsI-coated triple-GEM detector with finely segmented pad readout, capable of resolving the circular shape of the Cherenkov blob thus improving the particle identification power.<sup>77</sup>

Featuring full particle identification, the technique named ring imaging Cherenkov (RICH) exploits the photons emitted by fast charged particles in radiators; either by reflection in a mirror or by proximity focusing, the photons

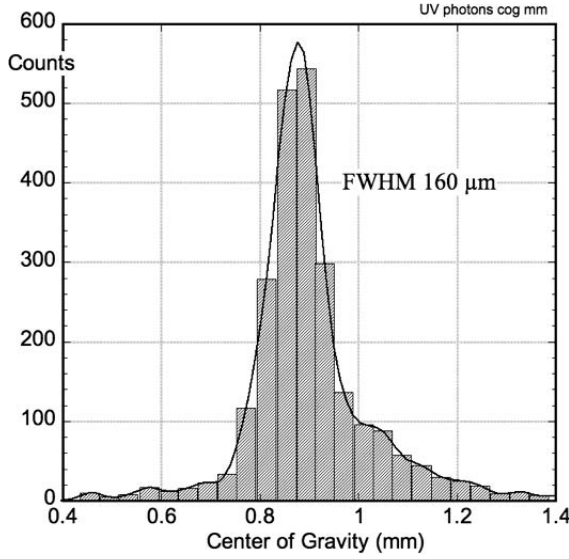


Fig. 37. Single UV photon localization accuracy.<sup>74</sup>

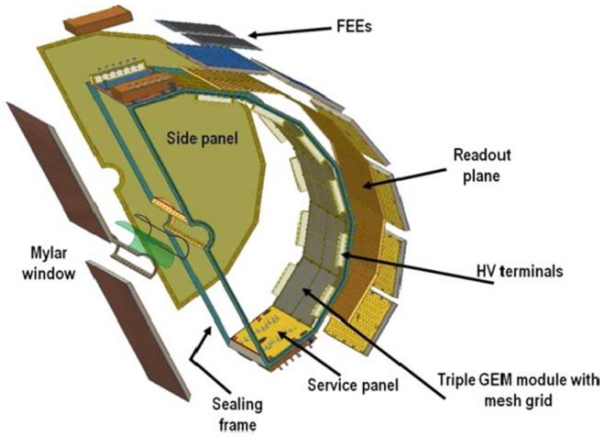


Fig. 38. Schematics of the PHENIX HBD.<sup>76</sup>

form a ring pattern whose radius correlated with the particle velocity.<sup>78</sup> Detectors making use of multiwire chambers have been successfully operated in experiments; one example is the COMPASS RICH-1 at CERN.<sup>79</sup> The detector is undergoing an upgrade to operate at the increased LHC luminosity; systematic research comparing various geometries led to the choice of a hybrid design, with two cascaded thick-GEM multipliers followed by a MICROMEAS as the final stage of amplification (Fig. 39).<sup>80</sup> This geometry ensures stable operation at the high gains needed for single photoelectron detection while reducing to about 3% the ion feedback to

F. Sauli

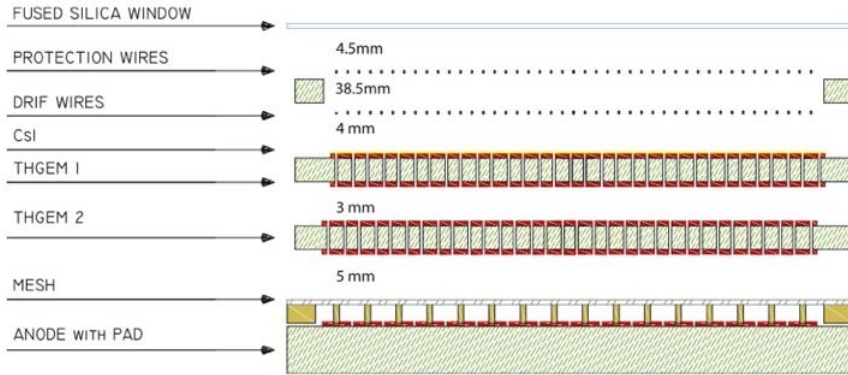


Fig. 39. Schematics of the hybrid GEM-MICROMEKAS detector for the COMPASS RICH-1 upgrade.<sup>82</sup>

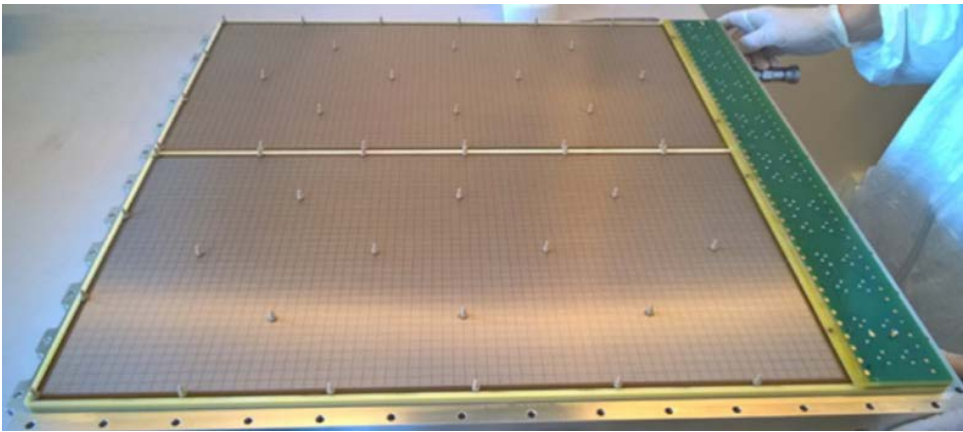


Fig. 40. A double-hybrid module for the COMPASS RICH upgrade during assembly; the pillars ensure a constant gap between MICROMEKAS and the nearest thick-GEM.<sup>82</sup>

the CsI photosensitive layer deposited on the top electrode of the first multiplier. Figure 40 shows the hybrid modules under construction<sup>81</sup>; Fig. 41 is an example of the Cherenkov ring recorded with the upgraded detector.<sup>80</sup> The average number of detected photons varies from 2 to 10 depending on the Cherenkov angle, with a single-photon angular resolution better than 2 mrad rms (Fig. 42).<sup>81</sup>

### 6.5. Plasma diagnostics

The very high-rate capability of GEM-based detectors permits 2D imaging of intense X-ray flux for fusion plasma diagnostics; images of X-ray emission are recorded with a pinhole GEM camera on a matrix of readout pixels, 2 mm<sup>2</sup> each, at rates exceeding 4 MHz per pixel.<sup>83</sup> Figure 43 is an example of a 2D image

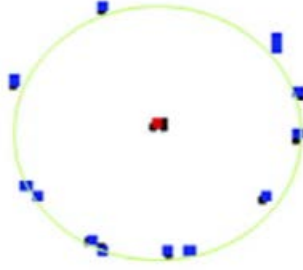


Fig. 41. A photon ring recorded with the COMPASS-1 upgraded RICH.<sup>80</sup>

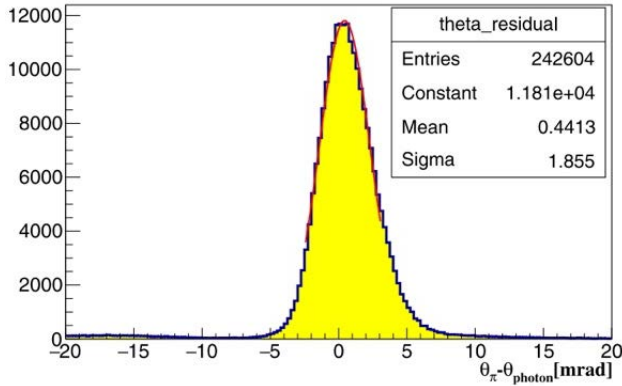


Fig. 42. Single-photon resolution.<sup>81</sup>

of the plasma source in presence of an estimated neutron and gamma flux above  $10^6$  MHz.<sup>84</sup>

A triple-GEM pinhole camera with an active area of  $10 \times 10$  cm<sup>2</sup> and  $12 \times 12$  pixels readout is used to record 2D images of high-temperature toroidal plasmas at the Korea Institute of Science and Technology (KAIST). The detector works in the photon counting mode and can acquire up to 60 frames at a 1 kHz sampling frequency. Figure 44 is a tangential image of the photon counting levels for a plasma shot.<sup>85</sup> A similar device, using a triple-GEM detector with 1D projective strips readout has been developed to monitor the plasma radiation at the joint European torus (JET).<sup>86</sup>

### 6.6. X-Ray polarimetry

The polarization of X-rays emitted by celestial sources is important information for the investigation of their nature. Micro-pattern detectors, with their high efficiency and good tracking capabilities, permit to measure the polarization of X-rays in the keV energy range. At these energies, the interaction of a photon with a gas molecule

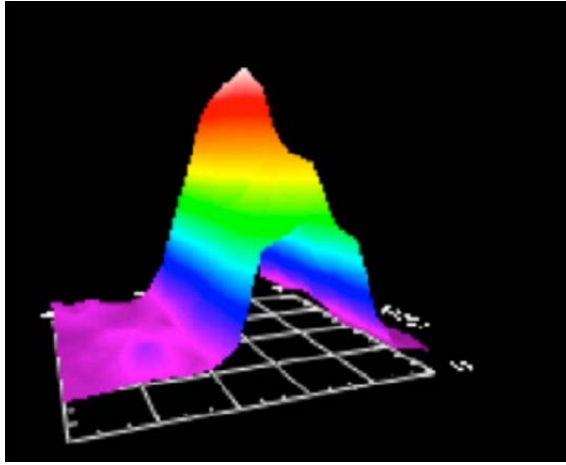


Fig. 43. 2D plot of soft X-rays plasma activity.<sup>84</sup>

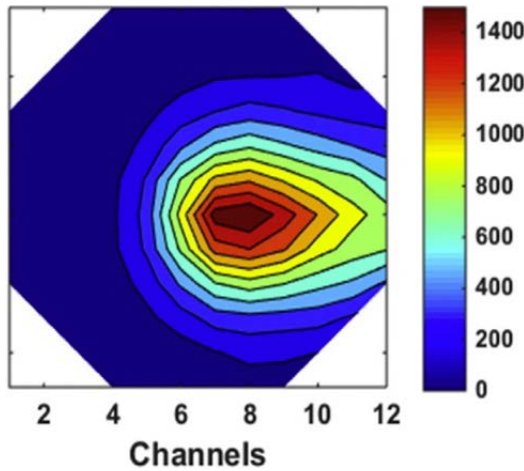


Fig. 44. Photons counting levels for a plasma shot.<sup>85</sup>

results in the emission of an electron almost perpendicularly to the incoming photon direction and the plane of its electric field; a measurement of the emission angle provides information on the polarization of the source.

The structure of the gas pixel polarimeter is shown in Fig. 45.<sup>87</sup> Photons interact in the drift volume; the ionization trails of released photoelectrons are amplified by a GEM electrode and recorded with a custom-made solid-state chip, directly collecting and encoding the charge on a matrix of  $\sim 50 \mu\text{m}$  hexagonal sensors. Matching the readout pitch, the GEM electrode is realized on a thin, metal-coated polymer foil with laser-drilled holes at  $50 \mu\text{m}$  pitch.<sup>88</sup> Figure 46 shows an example of electron track released by 5.9 keV X-rays and scattering in the He-based gas; the width

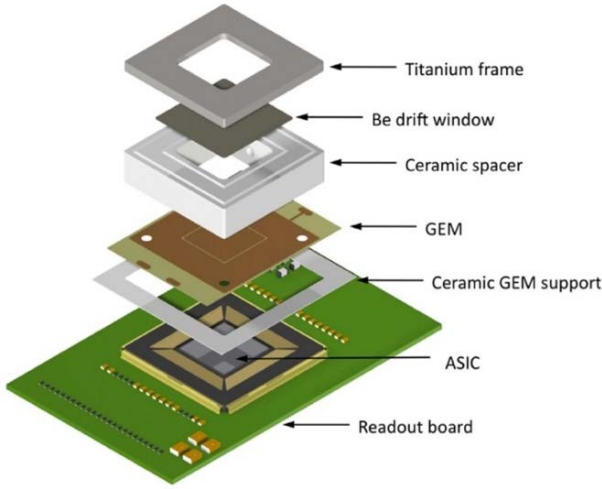


Fig. 45. The gas pixel detector assembly.<sup>88</sup>

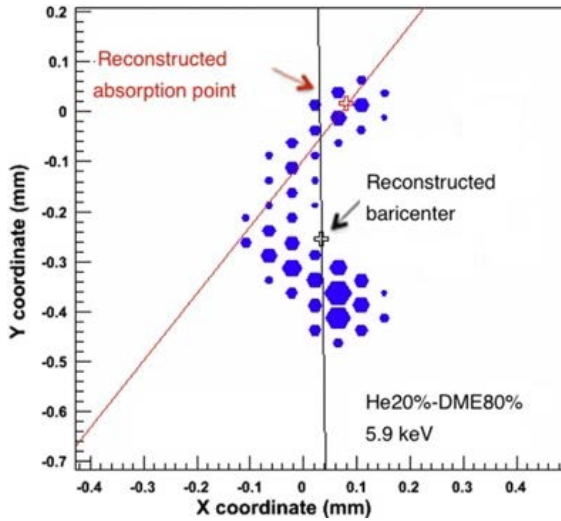


Fig. 46. A recorded 5.9 keV photoelectron track.<sup>88</sup>

of the pixels in the image is proportional to the charge recorded. The largest ionization loss at the end of the range of the electron permits to reconstruct the interaction point and then the angle of emission. Measured exposing the detector to a polarized photon beam, Fig. 47 is an example of a modulation function for 3.7 keV photons as a function of the angle of the detector with respect to the beam.<sup>88</sup>

Featuring a set of three gas pixel detectors, the imaging X-ray polarimetry explorer (IXPE) is due to be launched in late 2021 to perform polarization

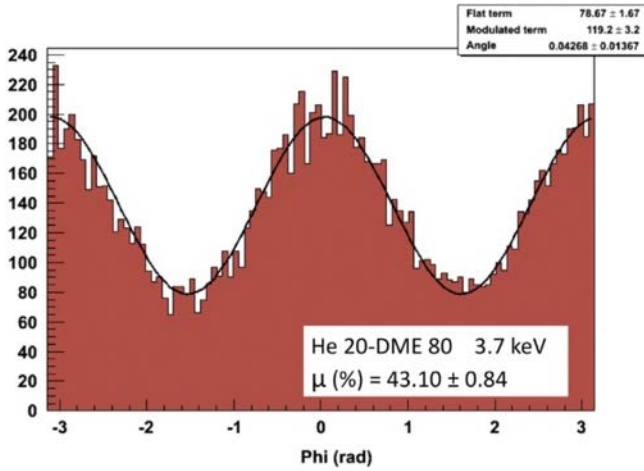


Fig. 47. Modulation of the reconstructed angles for polarized 3.7 keV X-rays.<sup>88</sup>

measurements in the 2–8 keV band, complemented with imaging, spectroscopy and timing capabilities.<sup>89</sup>

## 7. Cryogenic Dual-Phase Detectors

Gaseous devices, even at high pressures, do not have sufficiently large cross-sections for the detection of hypothetical events such as WIMPs, dark matter, axions, galactic neutrinos. Liquefied noble gases permit the implementation of larger masses; the small amount of ionization released by rare events, however, sets limits to direct charge detection. While charge multiplication has been sporadically observed in liquids, it is not sufficiently stable to ensure amplification. A solution has been found with the development of dual-phase devices, where ionization electrons released in the liquid volume are extracted into a gas layer and can be amplified and detected. For an exhaustive review of gaseous and dual-phase devices and their use in the detection of the rare process, see Ref. 90.

Dual-phase detectors exploit two fundamental features: a field-assisted electron extraction from the liquid, and a high gain operation of gaseous devices at cryogenic temperatures. Both processes have been extensively studied in the course of the development of the new generations of micro-pattern devices.<sup>91,92</sup> Figure 48 is an example of gain measured as a function of voltage in xenon, krypton and argon with a triple-GEM detector in a dual-phase device.<sup>91</sup>

As a scaled-up version of GEM, the LEM has been used to instrument an argon dual-phase detector. The prototype had a 10 cm thick LA drift volume; all materials for the assembly are selected to permit operation at a very low temperature.<sup>50</sup> Electrons released by ionization in the sensitive volume drift in the liquid are extracted into the gas phase and amplified by the LEM structure; the charge is detected and recorded on perpendicular strips on the anode plane. The liquid argon volume was

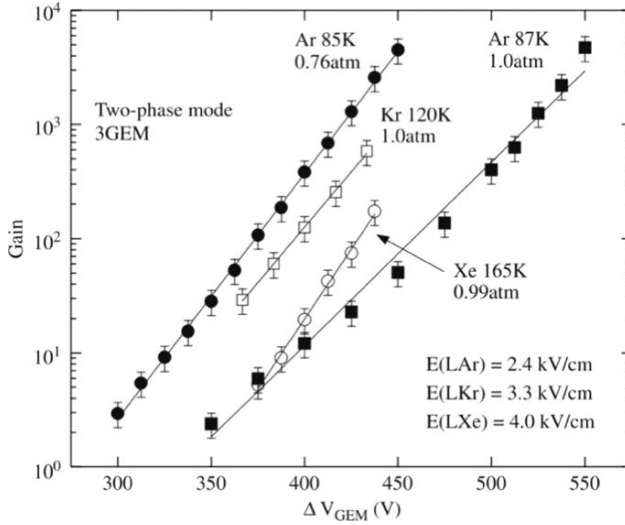


Fig. 48. Dual-phase triple-GEM gain as a function of the voltage applied in noble gases at cryogenic temperatures.<sup>91</sup>

progressively extended to 200 L, with a drift length of 60 cm and an active area of  $40 \times 76 \text{ cm}^2$  (Fig. 49).<sup>93</sup> The experience acquired with the prototypes served as the basis for the realization of a larger device, a  $3 \times 1 \times 1 \text{ m}^3$  (4.2 tons) dual-phase LA LEM-TPC (Fig. 50), designed for the deep underground neutrino experiment (DUNE).<sup>94</sup> Five photomultipliers, coated with wavelength shifters and mounted underneath the TPC field cage, detect the primary argon scintillation light, providing the time reference for the interaction.

## 8. Optical Imaging Detectors

The devices described in previous sections exploit collisional multiplication in high electric fields to increase the primary ionization charge and permit electronic detection. Photons are, however, copiously emitted both in the primary interactions and as an outcome of electron–molecule collisions, in a process named scintillation or luminescence. The emissions span over a wide range of wavelengths, depending on the nature, physical conditions of the medium and applied fields; in mixtures, the insurgence of a multitude of energy transfer processes complicates the issue further. For a review, see for example, Chap. 5 in Sauli’s book on gaseous radiation detectors.<sup>29</sup>

While the prominent photon emission is in the far and vacuum UV regions for most gases, requiring the use of wavelength shifters for detection, some molecules de-excite emitting photons at wavelengths close to or in the visible range, permitting direct optical detection of radiation using photography or solid-state cameras. The low photoionization threshold vapors used in RICH counters, TMAE and TEA, with secondary emission spectra centered around 460 and 260 nm, respectively, have

F. Sauli

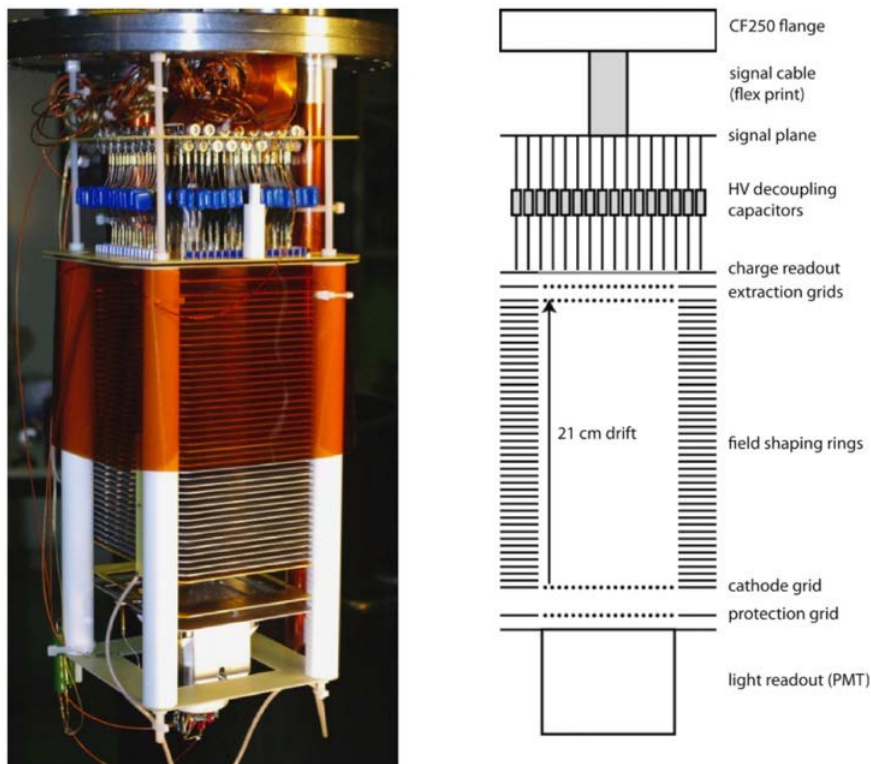


Fig. 49. The prototype drifts dual-phase LEM-TPC before insertion in the cryostat.<sup>95</sup>

been exploited for imaging in early works.<sup>97</sup> More recently, carbon tetrafluoride ( $\text{CF}_4$ ) has been demonstrated to have abundant emission in the visible range, with a peak around 650 nm, both pure and in admixtures with noble gases and a wide range of pressures.<sup>98–100</sup>

Detectors using cascaded GEMs are particularly well suited for optical imaging applications since they permit to reach high gains and can be directly viewed through a glass window.<sup>101</sup> The last GEM can be operated in the electron collection mode; alternatively, the anode can be a mesh with good optical transparency or a window coated with a semi-transparent resistive layer such as indium tin oxide (ITO) to collect the electron charge. This has opened a wide range of applications in fields where the modest data acquisition rates of commonly available optical recording systems are not limiting factors, as fluorescence elemental analysis<sup>102, 103</sup> and soft X-ray tomography.<sup>104</sup>

Optical readout systems are attractive to record low-rate events in large volume TPCs, a method developed by several research groups. Figure 51 is an example of a hadronic shower recorded in a charged particles beam at CERN with a small-sized optical triple-GEM-TPC using a high-resolution CCD camera.<sup>105</sup>

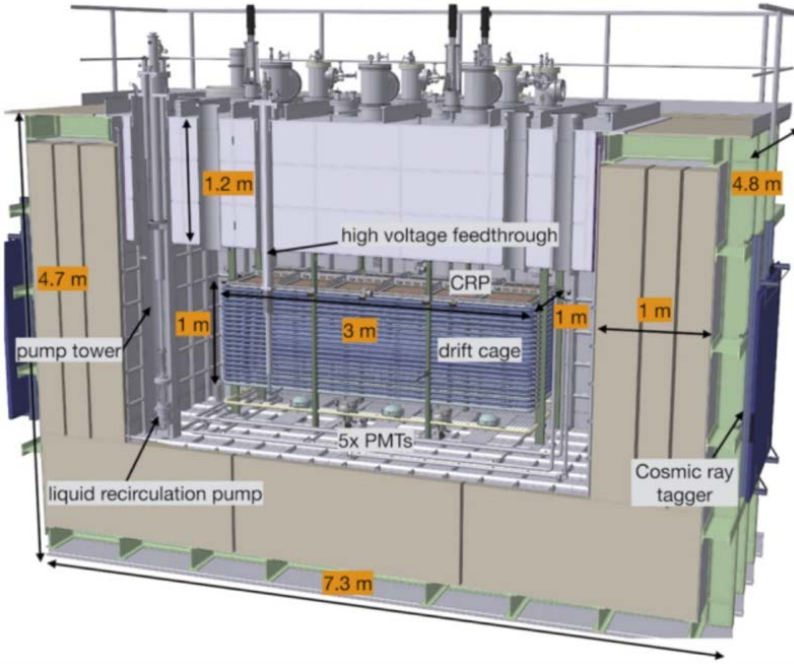


Fig. 50. The 4.2 tons dual-phase liquid argon LEM-TPC for DUNE.<sup>96</sup>

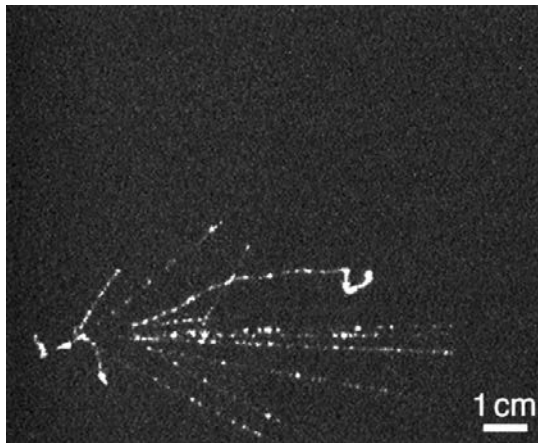


Fig. 51. Hadronic shower recorded with the optical GEM-TPC.<sup>105</sup>

GEM-TPCs with fruity names as ORANGE and LEMOn are developed by the Gran Sasso Science Institute (GSSI) as prototypes for larger devices aiming at dark matter searches (Fig. 52).<sup>106</sup> Figure 53 (left) is an example of tracks recorded with the detector exposed to an Am-Be source; the right plot is the result of a simple algorithm for particle identification based on ionization density.<sup>106</sup>

- 3D printed gas box
  - 3D printed field cage with metallic rings
  - Semi-transparent cathode (wire mesh)
- |     |                  |
|-----|------------------|
| (A) | Field Cage       |
| (B) | PMT              |
| (C) | Adaptable bellow |
| (D) | CMOS camera      |

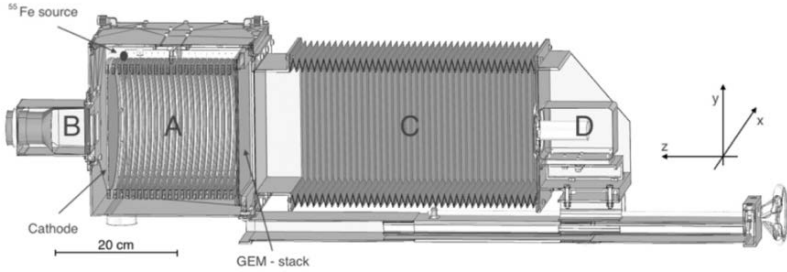


Fig. 52. The LEMOn optical GEM-TPC.<sup>107</sup>

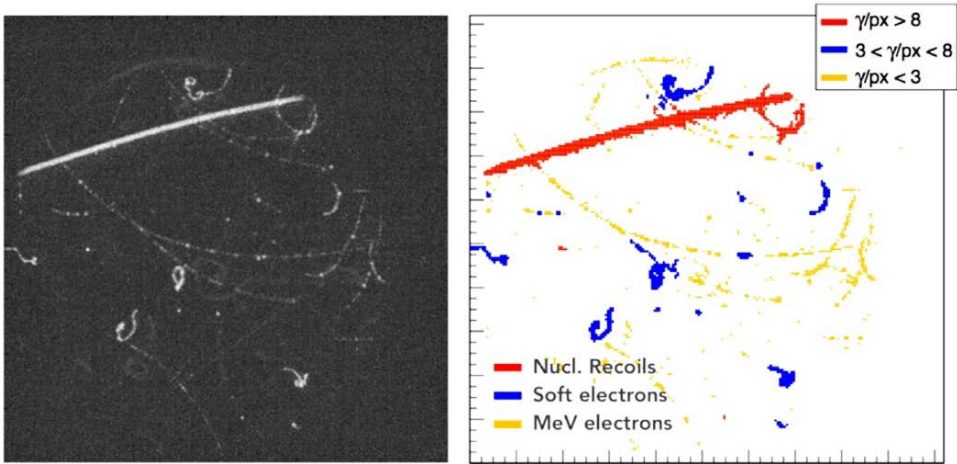


Fig. 53. Example of tracks recorded on exposure to an Am–Be source.<sup>106</sup>

As common CCD frame rates, kHz at best is much slower than the electrons' drift time, present-generation optical TPCs provide only 2D projected images of events, lacking depth. The information is often complemented using one or more photomultipliers, providing a fast signal on the event, that can be used for triggering purposes; if capable of detecting the scintillation of the primary interaction, they also provide the time reference. Various methods have been developed to provide a full 3D image of events: the correlation between image and charge, recorded independently on anodic strip,<sup>108</sup> and between clusters in the image and PM signals.<sup>109</sup> A substantial breakthrough of the technology would be allowed by the availability of streak cameras capable of recording images at 100 ns intervals or faster.

## 9. Summary and Conclusions

The introduction in recent years of innovative radiation sensors, collectively named MPGDs, providing sub-mm localization accuracies and capable of operating at high radiation fluxes, as well as and their use in various applied fields have been summarized in this note. For more exhaustive coverage of the subject, the reader is referred to the recent book on the subject by Sauli.<sup>5</sup> Motivated by the increasingly tough requirements of particle physics and astrophysics, dedicated structures have been developed having the common features of high reliability and low cost needed for large experimental setups. A CERN-based worldwide collaboration, RD51, has been established<sup>110,111</sup> and includes at the time of writing close to 90 contributing institutions; the collaboration holds regular workshops and meetings owing to a large number of interested researchers and the variety of perspective applications, the field is in continuing evolutions, with new or improved devices introduced uninterruptedly. The concurrent development of highly integrated sensing electronics and, for optical devices, of faster and higher resolution image recorders fosters the rapid development of the new technology.

## References

1. G. Charpak, R. Bouclier, T. Bressani, J. Favier and C. Zupancic, *Nucl. Instrum. Methods* **62**, 262 (1968).
2. A. Oed, *Nucl. Instrum. Methods Phys. Res. A* **263**, 351 (1988).
3. J. F. Clergeau *et al.*, *Nucl. Instrum. Methods Phys. Res. A* **471**, 60 (2001).
4. C. Budtz-Jorgensen *et al.*, *Proc. SPIE* **5165**, 139 (2004).
5. F. Sauli, *Micro-Pattern Gaseous Detectors: Principles of Operation and Applications* (World Scientific, Singapore, 2021).
6. Y. Giomataris, P. Rebourgeard, J. P. Robert and G. Charpak, *Nucl. Instrum. Methods Phys. Res. A* **376**, 29 (1996).
7. F. Sauli, *Nucl. Instrum. Methods Phys. Res. A* **386**, 531 (1997).
8. F. Angelini *et al.*, *Nucl. Instrum. Methods Phys. Res. A* **335**, 69 (1993).
9. R. Bellazzini *et al.*, *Nucl. Instrum. Methods Phys. Res. A* **424**, 444 (1999).
10. P. Rehak, G. C. Smith, J. B. Warren and B. Yu, *IEEE Trans. Nucl. Sci.* **47**, 1426 (2000).
11. A. Ochi, T. Nagayoshi, S. Koishi, T. Tanimori, T. Nagae and M. Nakamura, *Nucl. Instrum. Methods Phys. Res. A* **471**, 264 (2001).
12. P. Colas, I. Giomataris and V. Lepeltier, *Nucl. Instrum. Methods Phys. Res. A* **535**, 226 (2004).
13. G. Charpak, J. Derré, Y. Giomataris and P. Rebourgeard, *Nucl. Instrum. Methods Phys. Res. A* **478**, 26 (2002).
14. J. Derré and J. Giomataris, *Nucl. Instrum. Methods Phys. Res. A* **477**, 23 (2002).
15. V. Peskov, P. Martinengo, E. Nappi, R. Oliveira, P. Pietropaolo and P. Picchi, *J. Instrum.* **7**, C01005 (2012).
16. J. Galán *et al.*, *Nucl. Instrum. Methods Phys. Res. A* **732**, 229 (2013).
17. M. Chefdeville, Y. Karyotakis, T. Gerialis and M. Titov, *Nucl. Instrum. Methods Phys. Res. A* **824**, 510 (2016).
18. T. Alexopoulos *et al.*, *Nucl. Instrum. Methods Phys. Res. A* **640**, 110 (2011).
19. C. Bernet *et al.*, *Nucl. Instrum. Methods Phys. Res. A* **536**, 61 (2005).

20. P. Abbon *et al.*, *Nucl. Instrum. Methods Phys. Res. A* **779**, 69 (2015).
21. F. Thibaud, P. Abbon, V. Andrieux, M. Afrenville and E. Al, *J. Instrum.* **9**, C02005 (2014).
22. I. Gnesi, *J. Instrum.* **15**, C09019 (2020).
23. O. Sidiropoulou *et al.*, *Nucl. Instrum. Methods Phys. Res. A* **845**, 293 (2017).
24. M. Balikina *et al.*, *Phys. Part. Nucl. Lett.* **18**, 323 (2021).
25. A. Acker *et al.*, *Nucl. Instrum. Methods Phys. Res. A* **957**, 163423 (2020).
26. B. Radics *et al.*, *Rev. Sci. Instrum.* **86**, 83304 (2015).
27. Y. Nagata *et al.*, *JPS Conf. Proc.* **18**, 011007 (2017).
28. D. Nygren and J. Marx, *Phys. Today* **31**, 46 (1978).
29. F. Sauli, *Gaseous Radiation Detectors: Fundamentals and Applications*, Vol. 9781107043 (Cambridge University Press, 2014).
30. N. Abgrall *et al.*, *Nucl. Instrum. Methods Phys. Res. A* **637**, 25 (2011).
31. D. Attié *et al.*, *Nucl. Instrum. Methods Phys. Res. A* **957**, 163286 (2020).
32. D. Bernard, *Nucl. Instrum. Methods Phys. Res. A* **718**, 395 (2013).
33. K. Morishima *et al.*, *Nature* **552**, 386 (2017).
34. Y. Wang *et al.*, *IEEE Trans. Nucl. Sci.* (2021), arXiv:2107.09841.
35. J. A. G. Lacarra, PhD Thesis, University Zaragoza (2011), arXiv:1102.1406v2.
36. S. Andriamonje *et al.*, *Nucl. Instrum. Methods Phys. Res. A* **481**, 120 (2002).
37. J. Pancin *et al.*, *Nucl. Instrum. Methods Phys. Res. A* **524**, 102 (2004).
38. J. Pancin *et al.*, *Nucl. Instrum. Methods Phys. Res. A* **592**, 104 (2008).
39. P. Serrano, D. Attié, D. Desforge, E. F. Ribas, F. Jeanneau and O. Limousin, *J. Instrum.* **11**, P04016 (2016).
40. F. Sauli, *Nucl. Instrum. Methods Phys. Res. A* **805**, 2 (2016).
41. S. Bachmann, A. Bressan, L. Ropelewski, F. Sauli, A. Sharma and D. Mörmann, *Nucl. Instrum. Methods Phys. Res. A* **438**, 376 (1999).
42. J. Benlloch *et al.*, *Nucl. Instrum. Methods Phys. Res. A* **419**, 410 (1998).
43. A. Bressan *et al.*, *Nucl. Instrum. Methods Phys. Res. A* **425**, 254 (1999).
44. S. Duarte Pinto *et al.*, A large area GEM detector, *IEEE Nuclear Science Symp. Conf.* (IEEE, 2008), pp. 1426–1432.
45. M. Inuzuka, H. Hamagaki, K. Ozawa, T. Tamagawa and T. Isobe, *Nucl. Instrum. Methods Phys. Res. A* **525**, 529 (2004).
46. T. Tamagawa *et al.*, *Nucl. Instrum. Methods Phys. Res. A* **560**, 418 (2006).
47. L. Periale *et al.*, *Nucl. Instrum. Methods Phys. Res. A* **478**, 377 (2002).
48. R. Chechik, A. Breskin, C. Shalem and D. Mörmann, *Nucl. Instrum. Methods Phys. Res. A* **535**, 303 (2004).
49. A. Breskin *et al.*, *Nucl. Instrum. Methods Phys. Res. A* **598**, 107 (2009).
50. A. Badertscher *et al.*, *Nucl. Instrum. Methods Phys. Res. A* **617**, 188 (2009).
51. S. Bachmann *et al.*, *Nucl. Instrum. Methods Phys. Res. A* **479**, 294 (2002).
52. A. Bondar, A. Buzulutskov, L. Shekhtman and A. Vasiljev, *Nucl. Instrum. Methods Phys. Res. A* **496**, 325 (2003).
53. K. Dehmelt (2015), arXiv:submit/1158752.
54. S. F. Biagi, *Nucl. Instrum. Methods Phys. Res. A* **421**, 234 (1999).
55. R. Veenhof, *Nucl. Instrum. Methods Phys. Res. A* **419**, 726 (1998).
56. V. Tikhonov and R. Veenhof, *Nucl. Instrum. Methods Phys. Res. A* **478**, 452 (2002).
57. C. Altunbas *et al.*, *Nucl. Instrum. Methods Phys. Res. A* **490**, 177 (2002).
58. G. Croci *et al.*, *Nucl. Instrum. Methods Phys. Res. A* **712**, 108 (2013).
59. A. Balla *et al.*, *Nucl. Instrum. Methods Phys. Res. A* **732**, 221 (2013).
60. H. Fenker *et al.*, *Nucl. Instrum. Methods Phys. Res. A* **592**, 273 (2008).
61. A. Amoroso *et al.*, *Nucl. Instrum. Methods Phys. Res. A* **824**, 515 (2016).

62. D. Abbaneo, M. Abbas and M. Abbrescia, *Nucl. Instrum. Methods Phys. Res. A* **918**, 67 (2019).
63. M. Abbas *et al.*, *Nucl. Instrum. Methods Phys. Res. A* **14**, 164104 (2020).
64. D. Abbaneo *et al.*, *IEEE Trans. Nucl. Sci.* **65**, 2808 (2018).
65. P. Schade and J. Kaminski, *Nucl. Instrum. Methods Phys. Res. A* **628**, 128 (2011).
66. B. Ledermann, J. Kaminski, S. Kappler and T. Müller, *IEEE Trans. Nucl. Sci.* **53**, 2936 (2006).
67. D. Attié *et al.*, *Nucl. Instrum. Methods Phys. Res. A* **856**, 109 (2017).
68. M. E. Janssen *et al.*, *Nucl. Instrum. Methods Phys. Res. A* **566**, 75 (2006).
69. M. Berger *et al.*, *Nucl. Instrum. Methods Phys. Res. A* **869**, 180 (2017).
70. F. V. Böhmer *et al.*, *Nucl. Instrum. Methods Phys. Res. A* **737**, 214 (2014).
71. J. Adolfsson, M. Ahmed, S. Aiola, J. Alme, T. Alt and E. Al, *J. Instrum.* **16**, P03022 (2021).
72. M. M. Aggarwal *et al.*, *Nucl. Instrum. Methods Phys. Res. A* **903**, 215 (2018).
73. C. Lippmann, *Nucl. Instrum. Methods Phys. Res. A* **824**, 543 (2016).
74. T. Meinschad, L. Ropelewski and F. Sauli, *Nucl. Instrum. Methods Phys. Res. A* **535**, 324 (2004).
75. I. Tserruya, K. Aoki and C. Woody, *Nucl. Instrum. Methods Phys. Res. A* **970**, 163765 (2020).
76. W. Anderson *et al.*, *Nucl. Instrum. Methods Phys. Res. A* **646**, 35 (2011).
77. K. Kanno *et al.*, *Nucl. Instrum. Methods Phys. Res. A* **819**, 20 (2016).
78. J. Séguinot and T. Ypsilantis, *Nucl. Instrum. Methods* **142**, 377 (1977).
79. P. Abbon *et al.*, *Nucl. Instrum. Methods Phys. Res. A* **631**, 26 (2011).
80. J. Agarwala *et al.*, *Nucl. Instrum. Methods Phys. Res. A* **912**, 158 (2018).
81. J. Agarwala *et al.*, *Nucl. Instrum. Methods Phys. Res. A* **952**, 161832 (2020).
82. J. Agarwala *et al.*, *Nucl. Instrum. Methods Phys. Res. A* **936**, 416 (2019).
83. D. Pacella *et al.*, *Rev. Sci. Instrum.* **72**, 1372 (2001).
84. D. Pacella, A. Romano, L. Gabellieri, F. Murtas and D. Mazon, *Nucl. Instrum. Methods Phys. Res. A* **720**, 53 (2013).
85. I. Song *et al.*, *Curr. Appl. Phys.* **16**, 1284 (2016).
86. M. Chernyshova *et al.*, *J. Instrum.* **13**, C08001 (2018).
87. R. Bellazzini *et al.*, *Nucl. Instrum. Methods Phys. Res. A* **510**, 176 (2003).
88. R. Bellazzini *et al.*, *Nucl. Instrum. Methods Phys. Res. A* **720**, 173 (2013).
89. D. N. Lalla *et al.*, *Astropart. Phys.* **133**, 102628 (2021).
90. D. González-Díaz, F. Monrabal and S. Murphy, *Nucl. Instrum. Methods Phys. Res. A* **878**, 200 (2018).
91. A. Bondar, A. Buzulutskov, A. Grebenuk, D. Pavlyuchenko, R. Snopkov and Y. Tikhonov, *Nucl. Instrum. Methods Phys. Res. A* **556**, 273 (2006).
92. V. Chepel and H. Araújo, *J. Instrum.* **8**, R04001 (2013).
93. A. Badertscher *et al.*, *J. Instrum.* **8**, P04012 (2013).
94. B. Aimard *et al.*, *J. Instrum.* **13**, P11003 (2018).
95. A. Badertscher *et al.*, *Nucl. Instrum. Methods Phys. Res. A* **641**, 48 (2011).
96. C. Cuesta (2019), arXiv:1910.10115v1.
97. G. Charpak, J.-P. Fabre, F. Sauli, M. Suzuki and W. Dominik, *Nucl. Instrum. Methods Phys. Res. A, Accel. Spectrom. Detect. Assoc. Equip.* **258**, 177 (1987).
98. A. Pansky, A. Breskin, A. Buzulutskov, R. Chechik, V. Elkind and J. Va'vra, *Nucl. Instrum. Methods Phys. Res. A* **354**, 262 (1995).
99. A. Morozov *et al.*, *Nucl. Instrum. Methods Phys. Res. B* **268**, 1456 (2010).
100. M. Fraga, F. A. F. Fraga, S. T. G. Fetal, L. M. S. Margato, R. Ferreira Marques and A. Policarpo, *Nucl. Instrum. Methods Phys. Res. A* **504**, 88 (2003).

F. Sauli

101. F. Sauli, *Nucl. Instrum. Methods Phys. Res. A* **878**, 1 (2018).
102. A. L. M. Silva, R. Figueroa, A. Jaramillo, M. L. Carvalho and J. F. C. A. Veloso, *Spectrochim. Acta B* **86**, 115 (2013).
103. P. M. S. Carvalho *et al.*, *Eur. Phys. J. Plus* **136**, 423 (2021).
104. F. Brunbauer *et al.*, *J. Instrum.* **13**, T02006 (2018).
105. F. Brunbauer, Anwendungen von Eigenschaften szintillierender Gase in optisch ausgelesenen GEM-basierten Detektoren, Dissertation, Technische Universität Vienna (2018).
106. D. Pinci *et al.*, *Nucl. Instrum. Methods Phys. Res. A* **936**, 453 (2019).
107. V. C. Antochi *et al.*, *Nucl. Instrum. Methods Phys. Res. A* **999**, 165209 (2021).
108. F. M. Brunbauer *et al.*, *IEEE Trans. Nucl. Sci.* **65**, 913 (2018).
109. E. Baracchini *et al.*, *J. Phys. Conf. Ser.* **1498**, 12016 (2020).
110. M. Titov and L. Ropelewski, *Mod. Phys. Lett. A* **28**, 1 (2013).
111. RD51 Collab., Development of micro-pattern gas detectors technologies (2021), <https://rd51-public.web.cern.ch>.